# 3 Atmospheric transport and evolution of Hunga water vapour and aerosols

**Lead authors**
Sergey Khaykin
Adam Bourassa

**Co-authors**
Valentina Aquila
Alexandre Baron
Landon Rieger
Alexei Rozanov
Rei Ueyama

**Contributing authors**
Elizabeth Asher
Slimane Bekki
Marie Boichu
Parker Case
Margot Clyne
Kimberlee Dube
David Flittner
Eilidh Hlady
Mahesh Kovilakam
Cheng-Cheng Liu
Marion Marchand
Yifeng Peng
Samuel Remy
Michelle L. Santee
Florent Tence
Xinyue Wang
Pengfei Yu
Jun Zhang
Zhihong Zhuo
Nelson Begue
Ewa M. Bednarz
Christoph Brühl
Simon Chabrillat
Peter Colarco
Lola Falletti
Raphael Grandin
Julien Jumelet
Nicolas Lebas
Gloria L. Manney
Luis F. Millán
Richard Querel
Tetsu Sakai
Takashi Sekiya
Simone Tilmes
Shingo Watanabe
Wandi Yu
Yunqian Zhu

**Cite this as:**

Khaykin, S., A. Bourassa et al. (2025): Atmospheric transport and evolution of Hunga water vapour and aerosols. In APARC, 2025: The Hunga Eruption Atmospheric Impacts Report [Yunqian Zhu, Graham Mann, Paul A. Newman, William Randel (Eds.)]. APARC Report No. 11, WCRP Report No. 10/2025, DOI: 10.34734/FZJ-2025-05240, available at `https://aparc-climate.org/publications/aparc-report-no-11/`.

## Key points

Chapter 3 focuses on the evolution of the Hunga aerosol and water vapour after the first month. By March 2022, the volcanic plume had become zonally distributed in the tropics and over the next two years became dispersed meridionally across the globe.

- The volcanic aerosol was transported globally and the perturbation lasted more than two years.
  - In two months (by March 2022) the aerosol covered essentially all of the tropics, reaching stratospheric aerosol optical depth values greater than 0.02 at 1 µm.
  - In five months (by June 2022) the bulk of Hunga aerosol had been transported to the southern mid-latitude stratosphere due to efficient winter transport; northward transport was much weaker and more sporadic during that season.
  - In six months (by July 2022) the global stratospheric aerosol optical depth, which was still dominated by the aerosol in the southern hemisphere, reached a maximum value of 0.01 at 1 µm, and then decayed with an e-folding time of 20 months. This is the largest aerosol optical depth caused by a volcanic eruption since Mt. Pinatubo in 1991.
  - It took over two years for the stratospheric aerosol optical depth to decay to pre-eruption levels. Throughout this time, the bulk of the aerosol remained below 30 km.
  - The Hunga-driven stratospheric aerosol perturbation era has ended with the eruption of Ruang volcano in April 2024.
- The water vapour was transported globally, rose to the mesosphere, and remained dispersed throughout the atmosphere after more than two years.
  - The global anomaly in stratospheric water vapour mass was more than 15% higher than climatology and 10% higher than immediately before the eruption.
  - Transport over the first year was similar to the aerosol transport pattern, extending across most of the tropics in two months (March 2022), and largely moving to the southern mid-latitudes in five months (June 2022).
  - The water vapour remained between 20–32 km altitude for the first nine months (until October 2022), partly because the $H_2O$-forced radiative cooling counteracted the upwelling.
  - After this point, the water vapour ascended rapidly and reached the stratopause by early 2023.
  - By 2024, the water vapour anomaly was largely confined to the mesosphere, above approximately 50 km, and mostly at mid- and high latitudes.
- The aerosol particle size grew rapidly over less than a month to an effective radius of 0.4 µm and remained roughly constant over two years.
  - Balloon-borne measurements of the aerosol size distribution across the tropics and mid-latitudes show aerosol effective radius values of 0.4 µm in the Southern Hemisphere concurrent with the transport of the bulk aerosol.
  - Aerosol effective radius values in the Northern Hemisphere only reach 0.2 µm due to weaker transport and mixing with the background distribution.
  - Elevated values of particle size remained roughly constant over two years while gradually sedimenting toward tropopause altitudes.
- Transport of the water vapour and aerosol to the poles was effectively blocked by the polar vortex edges in the first winters in both hemispheres, and entrained in the vortices in the following winters.
  - In the Southern Hemisphere, Hunga water vapour reached the Antarctic vortex edge by mid-June 2022 and was excluded from entering the vortex due to the strong transport barrier at the edge; water vapour was entrained in the developing vortex of 2023.
  - Similarly, in the Northern Hemisphere, Hunga water vapour pervaded mid-latitudes by the second fall after the eruption and was entrained into the 2023/2024 vortex as it developed.

  - While the bulk of the aerosol did not penetrate the Antarctic vortex in 2022, observations suggest the presence of subtle aerosol layers in the lowermost high-latitude stratosphere before the vortex onset.

- Satellite observations show remarkable agreement between available measurements of stratospheric water vapour, and unusually large differences in aerosol extinction.
  - Available satellite observations of stratospheric water vapour use widely different measurement techniques yet agree in derived values of stratospheric mass anomaly to a remarkable degree of accuracy (less than 10% difference) throughout the two-year dispersion of the plume.
  - Large differences are observed in comparisons between aerosol measurements from satellites. The SAGE III/ISS measurements are the most accurate. Differences with other observations are often 50% and sometimes up to 100%. A main driver of these differences is systematic effects of the assumed particle size distribution in the limb scatter retrieval algorithms.

- Models simulate the global and vertical transport patterns of aerosols and water vapour reasonably well.
  - Models simulate the southward transport and vertical separation of the volcanic aerosol and water vapour quite well, indicating reasonably good representation of the large-scale circulation, polar vortex dynamics, and aerosol gravitational settling.
  - All models simulate smaller values of the Hunga perturbations in global stratospheric aerosol optical depth and water vapour compared to observations, but the decay rates of the perturbations are generally well simulated.
  - The cross-equatorial transport of the aerosol and water vapour perturbations from the Southern Hemisphere to the Northern Hemisphere is underestimated in all models.
  - All models simulate a rapid increase in effective radius after the eruption followed by a decrease as the largest particles differentially settle out of the atmosphere. The peak radius varies across models, but all models agree on a simulated radius of 0.2–0.3 μm two years after the eruption.

## Contents

## Preamble

Chapter 3 describes the global meridional and vertical evolution of the Hunga sulfate aerosols and water vapour after the full zonal dispersion of the plume, which occurred about one month after the eruption. Section 3.1 documents the dispersion of water vapour and aerosol, and Section 3.2 describes the global evolution of aerosol size derived from satellite, balloon-borne, and ground-based observations. Section 3.3 focuses on the transport of Hunga materials to the polar regions, including the Arctic and Antarctic polar vortices. The uncertainties of satellite observations of the Hunga aerosols and water vapour are assessed in Section 3.4, which provides a detailed intercomparison between various satellite data sets. Finally, results from dedicated climate model simulations of the global transport and evolution of Hunga aerosol and water vapour, in comparison with the observations, are provided in Section 3.5.

## 3.1 Meridional dispersion of water vapour and aerosol

By mid-February 2022, approximately one month after the eruption, the Hunga water vapour and sulfate aerosols were spread zonally across the southern tropics (Khaykin et al. (2022) and Chapter 2 of this assessment). The subsequent meridional dispersion of sulfate aerosols can be seen in Figure 3.1a, which shows the daily zonal average of stratospheric aerosol optical depth (SAOD) as observed by the OMPS-LP satellite instrument. Two months after the eruption, the bulk of the aerosol extended between 25°S–10°N, with zonal-mean SAOD values greater than 0.02 at 997 nm. At that time, there was a measurable SAOD enhancement covering almost the entire tropics (30°S–20°N). While the first detections of Hunga aerosol plumes at southern mid-latitudes were reported at Lauder station, New Zealand (45°S) and Dumont d'Urville (DDU) French Antarctic station (67°S) three and four weeks after the eruption, respectively (Khaykin et al., 2022), the Hunga aerosol largely shifted towards southern mid-latitudes three months after the eruption, in mid-April. At this time, the southern stratosphere started to turn to the winter regime, enabling a more efficient transport from the tropical belt towards the extratropics across the stratospheric "surf zone" around 30°S (Polvani et al., 1995). By June (five months after the eruption), the bulk of Hunga aerosol had migrated to the southern mid-latitudes.

The transport of the Hunga aerosols to northern mid-latitudes was more gradual. Figure 3.1a shows that the enhanced SAOD progressed towards the northern edge of the tropics within three months following the eruption. This was followed by several episodes of in-mixing into the northern extratropics in April 2022 and during November 2022 to January 2023 (Khaykin et al., 2024). These processes were reflected in the slow increase of Northern Hemisphere SAOD, peaking in mid-April 2022 and again in late 2022 (red curve in Figure 3.1c). The northbound dispersion of thin aerosol plumes between 22–25 km was captured by lidar observations across the northern extratropics (38°N–69°N) (Khaykin et al., 2020), whereas the larger-scale increase in the northern extratropical SAOD was not observed before early 2023 (Figure 3.1a). However, by far, the bulk of Hunga aerosol remained in the Southern Hemisphere.

The global SAOD perturbation reached its maximum value six months after the eruption, in July 2022, and subsequently entered a decay phase. During the second half of 2022, the SAOD decay rate in the Southern Hemisphere was faster than the global decay due to interhemispheric northbound transport (Figure 3.1c). One year after the eruption, in early 2023, the Hunga aerosol was spread across the entire Southern Hemisphere, and the SAOD decay rate in the Southern Hemisphere slowed and followed the global decay. By March 2024, more than two years post-eruption, the global and hemispheric SAOD time series converged and approached pre-eruption levels by mid-April 2024. The first significant post-Hunga SAOD perturbation, caused by the eruption of the Ruang stratovolcano in Indonesia on 16 April 2024 (Global Volcanism Program, 2024), ended the era of Hunga-driven stratospheric aerosol perturbation. Extrapolation of the stable decay of Hunga southern-hemispheric SAOD during early 2024 leads to an inferred total lifetime of the Hunga-induced stratospheric aerosol load of about 2.5 years, spanning from mid-January 2022 to mid-July 2024. The e-folding time of the global Hunga SAOD, taken from the peak in Figure 3.1c, is approximately 20 months. For comparison, the e-folding time of the extra-polar (polar regions excluded) SAOD perturbation caused by the Pinatubo eruption was 21 months, as inferred from the GloSSAC merged satellite dataset.

The meridional dispersion of the stratospheric columnar water vapour (SCWV) anomaly, derived from MLS measurements, is shown in Figure 3.1b as a daily zonal average, with the global anomaly reaching above 15% (Figure 3.1d). The observed transport was largely similar to that of the SAOD perturba-

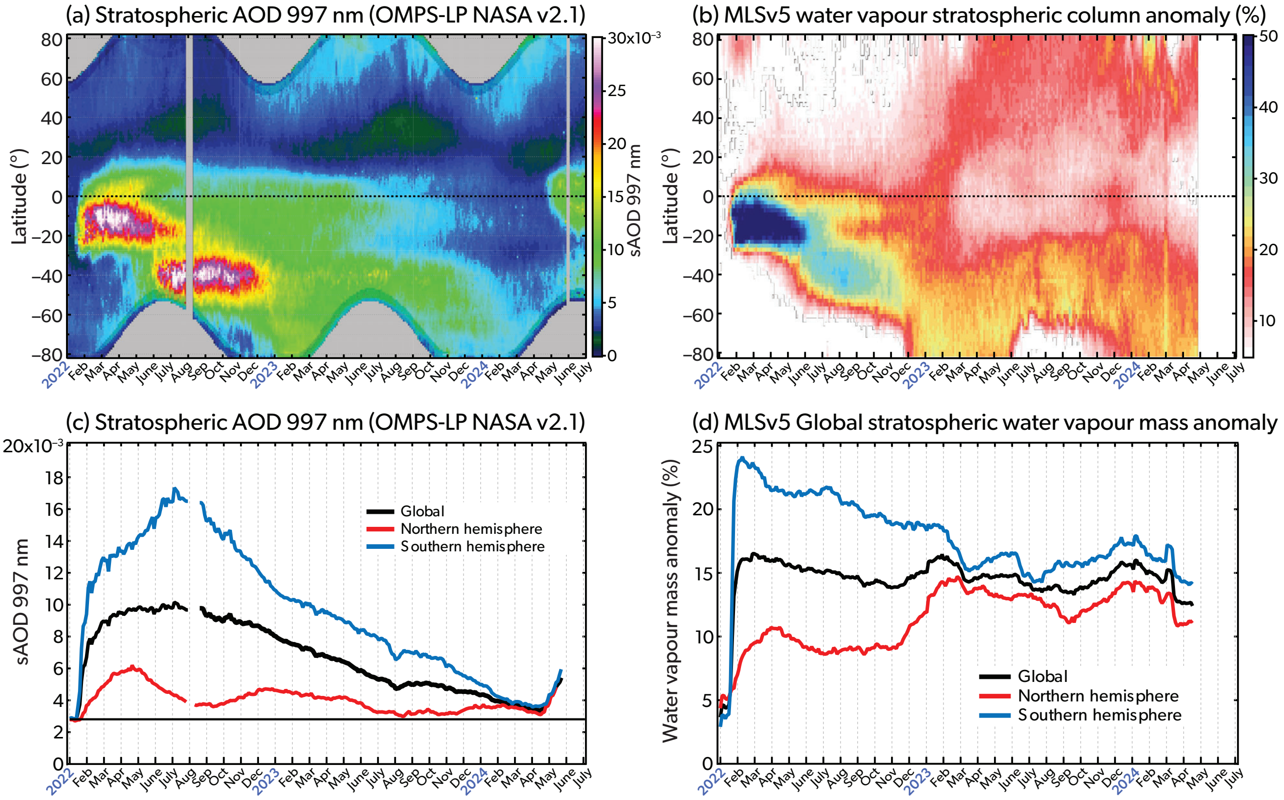

***Figure 3.1:*** *Meridional dispersion and evolution of Hunga aerosol and water vapour perturbation. (a) Stratospheric aerosol optical depth (SAOD) as a function of time and latitude from OMPS-LP NASA at 997 nm. (b) Water vapour anomaly as a function of time and latitude from MLS. (c) OMPS-LP NASA SAOD time series for global average, Northern Hemisphere, and Southern Hemisphere. (d) MLS water vapour anomaly time series for global average, Northern hemisphere, and Southern hemisphere. The anomaly is computed from deseasonalised MLS data prior to 2022.*

tion during the first four months, extending over 30°S–10°N by mid-May 2022. Small in-mixing events of Hunga moisture into the northern extratropics during March–April 2022 observed by MLS were confirmed by balloon soundings in China at 26.7°N (Xu et al., 2022).

A striking difference between the evolutions of the aerosol and water vapour distributions is that, while the Hunga sulfate aerosols experienced descent due to gravitational settling, the water vapour rose in altitude in the tropics within the deep branch of the Brewer–Dobson circulation. This led to vertical separation of the particulate and gaseous Hunga material (detailed below) and substantially modified their meridional transport pattern beginning in late 2022. While the aerosol perturbation remained largely restricted to the Southern Hemisphere, Figure 3.1b shows that in January 2023 the Hunga stratospheric moisture experienced a major episode of northward transport from the tropical pipe to the northern high latitudes. This striking transport can be linked to the seasonal dynamics of the Arctic stratospheric vortex, which was subject to a sudden stratospheric warming event in early 2023 (Newman et al., 2024). By the end of boreal winter 2023, the Hunga water vapour reached full planetary extent; however, at this point, most of the excess moisture was outside the tropics (Figure 3.1b). In the tropics, the anomaly remained mostly below 10% after March 2023 but experienced two measurable enhancements around June 2023 and November 2023, which can both be linked to distinct tropical tropopause temperature variations (not shown).

As with the stratospheric aerosol, the Hunga SCWV perturbation was predominantly in the Southern Hemisphere, where the anomaly from the climatological levels reached 24% shortly after the eruption and decreased to 22% by May 2022 due to cross-equatorial transport (Figure 3.1d). By March 2023, 14 months after the eruption, the hemispheric SCWV anomalies converged to the global anomaly of 15% to within 1%, indicating quasi-uniform global meridional dispersion of Hunga water vapour. This timeframe of 14 months is an indication of the global stratospheric mixing timescale, which has been uniquely provided by the Hunga eruption as a natural experiment on stratospheric composition.

The further evolution of the SCWV perturbation in the extratropics was driven by the dehydration in the Antarctic polar vortex during June–October 2023 through polar stratospheric clouds (PSCs) (Zhou et al., 2024; Millán et al., 2024), as well as by sub-seasonal dynamics of the Arctic polar vortex during boreal winter 2023/2024. By March 2024, water vapour in the tropics reached background levels; however, the global anomaly was only 7.7% lower than the maximum post-Hunga anomaly in late February 2022 (Figure 3.1d). Unlike the polar or tropical regions, the lifetime of excessive moisture in the midlatitude stratosphere is less constrained by vertical removal mechanisms.

As noted above and in Chapter 2, the differences in the meridional dispersion patterns of aerosols and water vapour are driven by their vertical separation. The vertical evolutions of the Hunga water vapour anomaly and sulfate aerosols for different latitudinal regions are shown in Figure 3.2. One month after the eruption, the bulk of the water vapour anomaly, ranging between 1–4 ppmv in the tropics (Figure 3.2b), was confined to altitudes between 20–30 km, which roughly corresponded to the vertical extent of the volcanic aerosol. During the first few months after the eruption, the upward propagation of the moist anomaly in the tropical upwelling was partly inhibited by radiative cooling caused by the excessive moisture (Sellitto et al., 2022; Schoeberl et al., 2022). The ascent of the tropical water vapour anomaly began in October 2022 and reached the stratopause by early 2023. The acceleration of tropical upwelling in late 2022 can be associated with a change in the QBO phase. By early 2024, the extent of the water vapour anomaly exceeding 1 ppmv was entirely above the stratosphere and occupied a broad altitude layer in the mesosphere.

In contrast to the gaseous water, the aerosol particles were subject to gravitational settling, and the bulk of aerosols remained in the lower stratosphere, between 17–25 km altitude. The ultimate vertical separation of the aerosol and water vapour perturbations at all latitude bands occurred approximately one year after the eruption. While the aerosols gradually settled to the tropopause level, the water vapour anomaly persisted in the middle stratosphere throughout 2022. The steep rise in altitude of the hydrated layer in April 2023 is associated with transport from outside the tropical pipe, as noted above. In the northern extratropics, the water vapour anomaly did not appear before November 2022 and then largely replicated the vertical evolution pattern seen in the south. Variations of the anomaly in the mesosphere are likely linked to solar activity through molecular dissociation by Lyman-$\alpha$ radiation and formation of noctilucent clouds (Sonnemann and Grygalashvyly, 2005). By early 2024, two years after the eruption, the water

(a) $H_2O$ anomaly and extinction ratio, 30°N–60°N

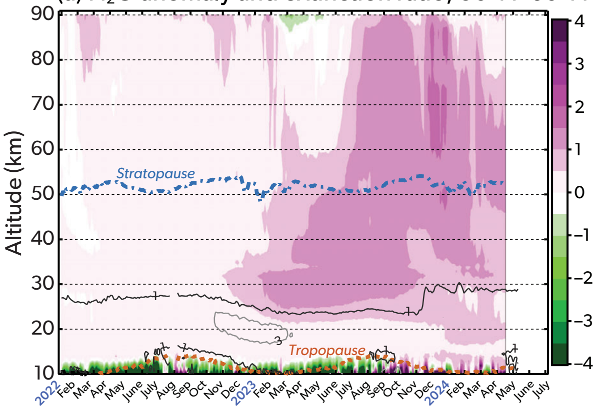

(b) $H_2O$ anomaly and extinction ratio, 30°S–30°N

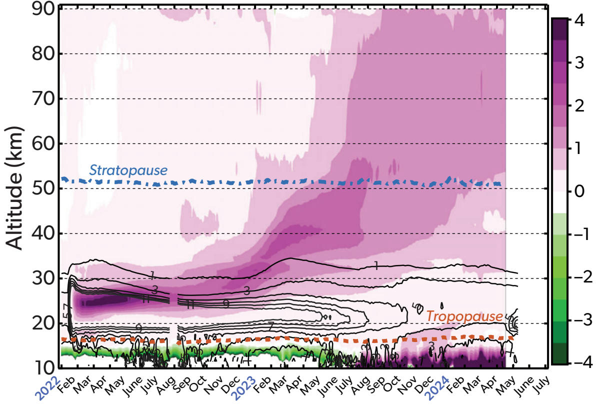

(c) $H_2O$ anomaly and extinction ratio, 60°S–30°S

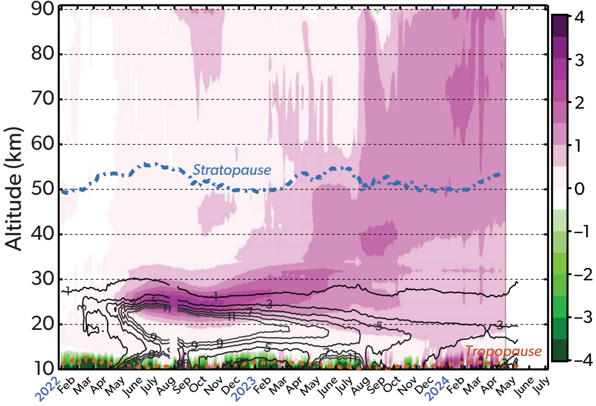

***Figure 3.2:*** *Vertical evolution of the water vapour absolute anomaly and aerosol perturbation from MLS and OMPS-LP. Water vapour anomaly (shades) and aerosol extinction ratio (contours) as a function of time and altitude at different latitude bands: (a) 30°N–60°N, (b) 30°S–30°N, and (c) 60°S–30°S.*

vapour anomaly larger than 1 ppmv extended from the tropopause to the mesopause in the extratropics, whereas the aerosols had largely settled out of the stratosphere.

## 3.2 Evolution of sulfate aerosols

### *3.2.1 Aerosol growth and changes in the size distribution*

As noted in Chapter 2, the emitted $SO_2$ gas converted rapidly, within days, to sulfate aerosol droplets. Meanwhile, the UV-absorbing particles—likely ash—were observed only during the first week after the eruption and in relatively small amounts. Within a month, the Hunga aerosol already consisted of sulfate aerosol particles with a size distribution that was unexpectedly stable and characteristic of this eruption. Indeed, after the rapid growth phase (see Chapter 2), the particles stopped growing, unlike what has been measured in former major eruptions, e.g. the Pinatubo sulfates' modal radius up to 0.8 µm, as reported by Russell et al. (1996). Namely, the aerosol grew within a week from a typical stratospheric background radius centred around 0.15 µm to a narrower pseudo-lognormal size distribution with a modal radius of approximately 0.35 µm (e.g. Duchamp et al., 2023; Li et al., 2024).

Several complementary lines of observations corroborate this result. Balloon-borne *in-situ* profiles using the Portable Optical Particle Spectrometer (POPS) were able to assess the aerosol size in the early plume above La Réunion (see Chapter 2; Asher et al., 2023) and continued to monitor the microphysics of the plume with time and latitude from several stations (`https://csl.noaa.gov/projects/b2sap/`). These observations complement the SAGE III/ISS satellite measurements of the spectrum of aerosol extinction that allow for the retrieval of a single-mode lognormal size distribution using the methods presented in Wrana et al. (2021) and Knepp et al. (2024).

A convenient way of condensing the information on the aerosol size distribution is to compute the effective radius of the aerosol. Namely, the effective radius is the ratio of the third (volume) to the second (surface) moments of the size distribution. It represents a suitable proxy for the size distribution when calculating radiative properties of the aerosol and is a commonly retrieved quantity from optical satellite measurements. For a single-mode lognormal distribution with a known width, the effective radius relates to the modal radius with an analytic expression (Duchamp et al., 2023).

Figure 3.3 shows the evolution of the effective radius of the Hunga aerosol. The zonal mean of the SAGE III/ISS effective radius is displayed for four latitude bands, from northern to southern mid-latitudes, together with balloon-borne POPS profiles from La Réunion, France (21° S; Figure 3.3a), Hilo, Hawaii (19° N; Figure 3.3b), Lauder, New Zealand (45° S; Figure 3.3c), and Boulder, Colorado (40° N; Figure 3.3d). Although these two types of measurements use completely different techniques, the results agree well in terms of both magnitude and altitude of the effective-radius perturbation. The peak effective radius reached just above 0.4 µm in the early stage in the southern tropics. The larger particles are observed later in the southern mid-latitude reaching similar values of effective radius. In the northern hemisphere, the aerosol size does not show a large increase, with effective radius reaching up to approximately 0.2 µm. This is consistent with the observed transport of the bulk of the aerosol toward the southern hemisphere, and the mixing with the background aerosol in the northern mid-latitudes.

In addition to the satellite remote sensing and *in-situ* measurements, the size distribution of Hunga aerosols can be constrained by photometric ground observations from multiple stations of the worldwide AERONET network. A rapid growth is observed in the days following the eruption (see Chapter 2 for details), faster than that observed after the 1991 Pinatubo eruption (Boichu et al., 2023). Figure 3.4 shows that a distinct increase in aerosol peak radius of the calculated fine-mode volume size distribution ($r_{\text{peak}}$) to values in the range 0.3–0.5 µm was reported across the 23 AERONET stations of the Southern Hemisphere. This persisted until at least March 2024, in full agreement with SAGE III/ISS and POPS observations. Hence, despite a rapid growth in the post-eruption week—likely due to the exceptional abundance of water in the Hunga plume resulting from the phreatomagmatic nature of the eruption (interaction of water and magma)—the Hunga aerosols remained smaller than those reported after the Mt. Pinatubo eruption in 1991 (Boichu et al., 2023).

The Lauder station (New Zealand, 45° S) within the Balloon Baseline Stratospheric Aerosol Profiles project (B2SAP; `https://csl.noaa.gov/projects/b2sap/`) has been an ideal location for monitoring the fate of the Hunga aerosol plume microphysics with time. Observations from this station are representative of the volcanic aerosol that persisted in the southern mid-latitudes until 2024 (see Section 3.1). In Fig-

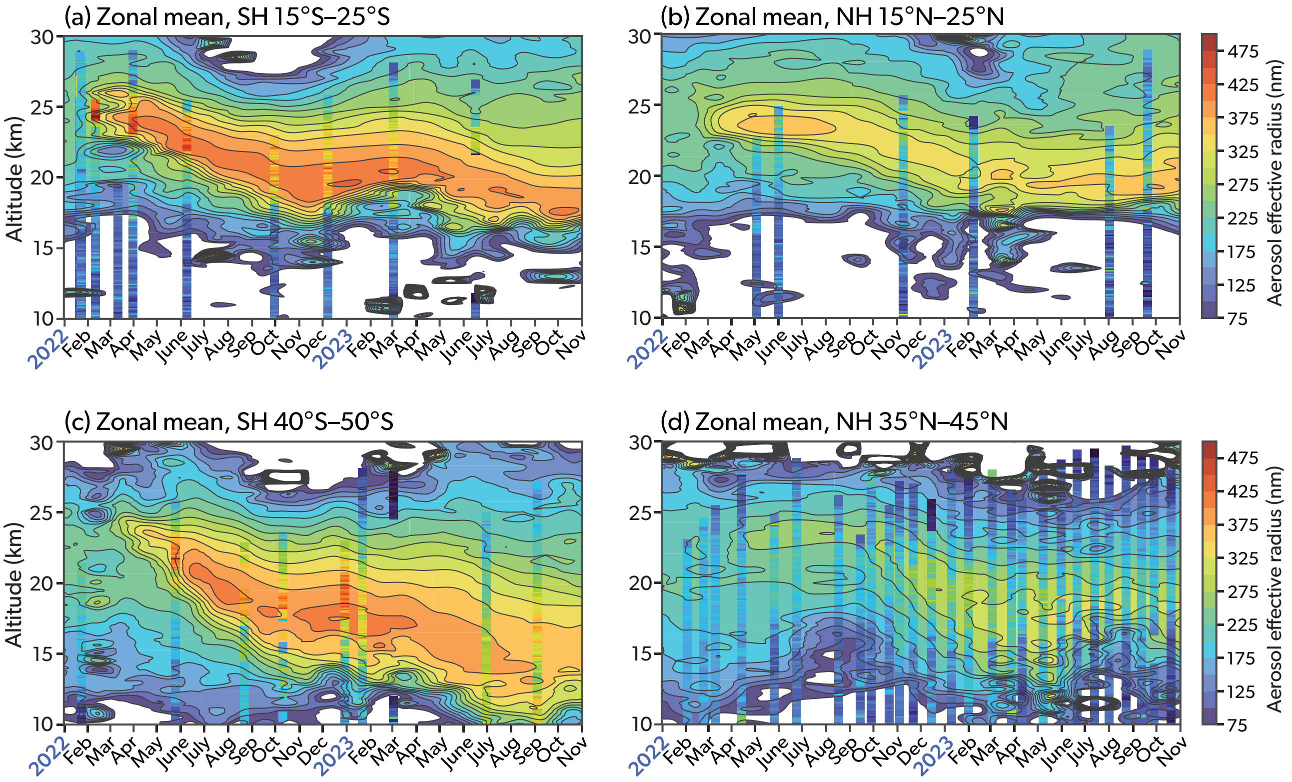

*Figure 3.3: Aerosol effective radius as a function of time and latitude in four latitude bands retrieved from SAGE III/ISS solar occultation spectra, with overlaid markers representing effective radius measured in situ by balloon sondes.*

ure 3.5, POPS-derived normalised aerosol surface size distributions are plotted in 6-month increments from January 2022 for two stratospheric regions (broadly defined as mid and lower stratosphere). The aerosol surface is both relevant for heterogeneous chemistry in the stratosphere and long-term radiative properties.

For the mid-stratosphere region, with potential temperature from 550 K to 750 K (approximately 22–28 km altitude at this latitude), the surface size distribution shifted toward larger sizes soon after the eruption. From background conditions with a modal radius below 0.1 µm, the perturbed distribution shifted to peak around 0.35 µm (Figure 3.5a, red–purple curve) during the first six months after the eruption. With time, this decreased to approximately 0.25 µm in early 2023 and remained relatively stable into 2024. At the end of 2024, this Hunga mode was fading away.

In the lower-stratosphere region, with potential temperature from 380 K to 550 K (approximately 14–22 km altitude at this latitude), a somewhat different particle evolution was observed. Six months after the eruption, the modal radius of the aerosol surface size distribution was centred at approximately 0.25 µm but increased with time to peak around 0.35 µm in 2023. By the end of 2024, a return toward background conditions (modal radius of approximately 0.11 µm) was observed (Figure 3.5b), with the perturbed mode decreasing in favour of a smaller mode (< 0.1 µm). These results from POPS profiles from Lauder demonstrate the sedimentation of larger particles, initially formed in the mid-stratosphere, to the lower stratosphere. This is further discussed in the following section.

### *3.2.2 Sedimentation of aerosol particles*

The SAGE III/ISS extinction and derived effective-radius profiles (Knepp et al., 2024) provide a clear picture of the particle sedimentation that occurred following the Hunga eruption. Figure 3.6 shows the time evolution of average profiles in the tropics between 10° S and 10° N. For the four months preceding the eruption (Panels A–B), the particle effective radius (shown in red) was approximately 0.25 $\mu$m for most of the lower stratosphere. In the months immediately following the eruption (Panels C-D), effective radius is approximately 0.4 $\mu$m with a peak near 25 km, which is consistent with the balloon-borne and ground-based results presented in the previous section. At this point in time, the extinction at 755 nm, shown in black, has a peak that is collocated with the peak in effective radius. From May to August 2022

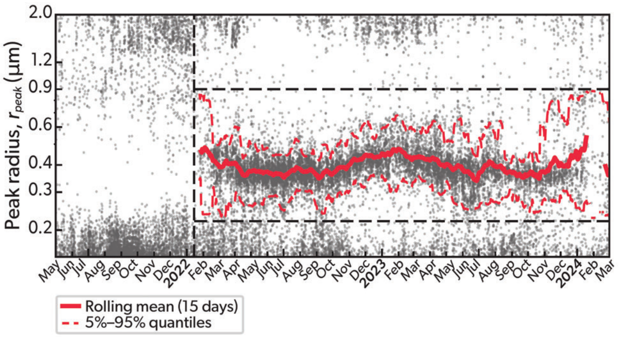

*Figure 3.4:* *Composite time series of aerosol peak radius ($r_{peak}$) ranging within the volcanic size range [0.22–0.90] µm at 23 AERONET stations of the Southern Hemisphere. $r_{peak}$ is the radius at the peak of the aerosol volume size distribution (fine mode). The thick red line shows the rolling median computed after the Hunga eruption (vertical dashed line) with a 15-day window, restricted to data points within the volcanic size range (black dashed lines). Dashed red lines indicate the 5% and 95% quantiles. Among the 23 AERONET stations, 11 are in the southern tropics (lat < 23.5° S) and 12 are in the southern mid-latitudes (up to 45.8° S). The stations include Niassa (Mozambique), American Samoa, Mount Chacaltaya (Bolivia), La Paz (Bolivia), Huancayo IGP (Peru), Lucinda (Australia), Windpoort (Namibia), Maïdo OPAR (Réunion Island), Learmonth (Australia), HESS (Namibia), SP-EACH (Brazil), Gobabeb (Namibia), PSDA Chile (Chile), Yerba Loca (Chile), Metsi (South Africa), Upington (Zambia), Fowlers Gap (Australia), Lake Lefroy (Australia), AU NSW Lidcombe (Australia), Univ. of Auckland (New Zealand), CEILAP–Neuquén (Argentina), Trelew (Argentina), and CEILAP–Comodoro (Argentina).*

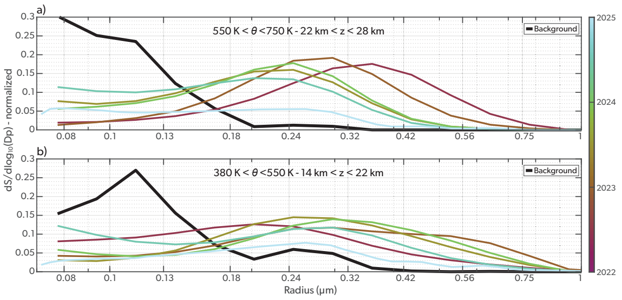

*Figure 3.5:* *Time evolution (6-month increments) of the resolved aerosol surface size distribution (normalised) measured in situ by balloon sondes from Lauder, New Zealand (45° S): (a) upper stratosphere (potential temperature 550–750 K, equivalent to 22–28 km), and (b) lower stratosphere (potential temperature 380–550 K, equivalent to 14–22 km).*

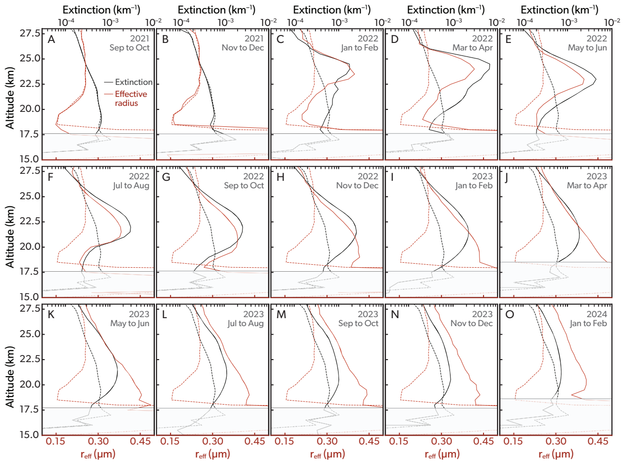

*Figure 3.6:* *Two-month average profiles of aerosol extinction (black, top axis) and effective radius (red, bottom axis) from SAGE III/ISS in the tropics (10° S–10° N), showing the descent of larger particles and the eventual altitude separation of the peak extinction and peak effective radius. In each panel, pre-eruption extinction (September–December) and radius profiles from late 2021 are shown as dashed curves for reference.*

(Panels E-F) this relationship between effective radius and extinction continues with both quantities having peaks that both drop and spread out in altitude. Past August 2022 (Panels G-O) there is a marked altitude separation between the extinction and effective radius peaks, with the extinction peak remaining near 22 km while the effective radius peak continues to drop. During this descent, the effective radius continues a slow increase, with values approaching 0.45 µm by September 2023. While the extinction peak remains near 22 km, it continues to broaden; coupled with the changes in effective radius this indicates a gradation of particle sizes as the larger particles sediment more rapidly.

### 3.2.3 Hunga aerosol in the long-term record

The longest continuous records of SAOD are provided by ground-based lidars operating within the Network for the Detection of Atmospheric Composition Change (NDACC) and merged satellite products. In order to compare the magnitude of Hunga-induced SAOD perturbation with that of past moderate and major eruptions, Figure 3.7 shows monthly-mean SAOD time series from two midlatitude and two tropical lidars sites located symmetrically with respect to the equator: Lauder (45° S), La Réunion (21° S), Mauna Loa (21° N) and Observatoire de Haute-Provence (OHP; 44° N), each compared with the Global Space-based Stratospheric Aerosol Climato-

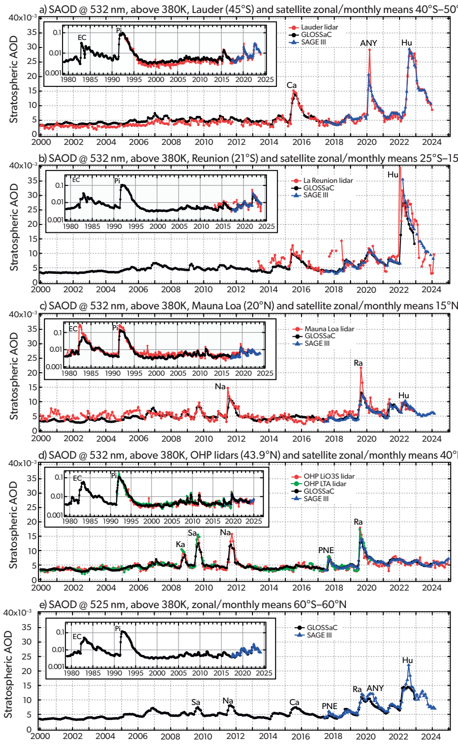

***Figure 3.7:*** *Time series of aerosol optical depth above the 380 K potential temperature level from ground-based lidars at different sites, compared with GloSSAC V2.21 merged satellite data and SAGE III/ISS observations zonally averaged within corresponding 10° latitude bands: (a) Lauder (45° S); (b) La Réunion (21° S); (c) Mauna Loa (21° N); (d) Haute-Provence (44° N); (e) Satellite quasi-global series within 60° S–60° N.*

logy (GloSSAC; Kovilakam et al., 2020) and zonally averaged SAGE III/ISS data for the respective latitude band.

The largest SAOD perturbation magnitude was recorded at La Réunion (21° S) in January 2022, which is expected given the site's location directly downwind of Hunga at nearly the same latitude (Figure 3.7b). As the bulk of Hunga aerosols was transported to the southern mid-latitudes in June 2022 (see Section 3.1), the peak of the SAOD perturbation at Lauder (45° S) was observed during June–July 2022 (Figure 3.7a). In both Southern Hemisphere lidar records, the magnitude of the Hunga perturbation is the largest observed since Mt. Pinatubo in 1991.

In contrast, the SAOD perturbation at Mauna Loa (21° N; Figure 3.7c), at the northern edge of the tropics, was relatively weak, with SAOD returning to pre-eruption levels before the end of 2023. At the northern mid-latitudes (Figure 3.7d), the OHP record shows a small increase in SAOD in late 2022, reflecting the gradual transport of Hunga aerosols to the northern extratropics (Section 3.1). The SAOD time series averaged for the full 60° S–60° N latitude range (Figure 3.7e), from GloSSAC and SAGE III/ISS, confirms that even on a near-global scale the Hunga SAOD perturbation is the largest observed in the post-Pinatubo era. However, even at these levels, the peak magnitude of the Hunga SAOD perturbation was approximately a factor of six smaller than that of Pinatubo.

## 3.3 Transport of volcanic material into the polar regions

This section focuses specifically on the transport of the volcanic aerosol and water vapour into the polar regions. This process is particularly important due to its potential for impact on the size and strength of the polar vortex, and perturbation of the vortex chemistry, including ozone loss.

### *3.3.1 Water vapour*

Manney et al. (2023) detailed the march of the Hunga water vapour plume towards the developing polar vortex in austral fall 2022. Figure 3.8 shows the global transport of the Hunga eruption water-vapour plume through 2023 as measured by MLS, using equivalent latitude as a coordinate to distinguish vortex from extra-vortex air. The bulk of the plume transported into the Southern-Hemisphere extratropics during 2022 remained between approximately 500 K and 800 K (about 50–10 hPa; 20–30 km altitude) and reached the vortex edge in early- to mid-June 2022 at those altitudes (Figures 3.8a–3.8b, 3.8f). By this time, the Antarctic stratospheric polar vortex—developing since April at these levels—had reached near-full strength and acted as an effectively impenetrable transport barrier, excluding Hunga water vapour from the 2022 vortex. Consequently, there was no discernible effect of Hunga water vapour on vortex processing in the 2022 Antarctic winter (Manney et al., 2023 and Chapter 5). Hunga-enhanced water vapour was able to reach the polar regions only after the springtime vortex breakup, in November 2022 at higher altitudes (Figure 3.8a) to December 2022 in the lower stratosphere (Figure 3.8b). By Southern-Hemisphere fall 2023, high Hunga-derived water vapour pervaded Southern-Hemisphere high latitudes (Figures 3.8a, 3.8b, 3.8i) and was entrained into the developing Antarctic vortex, with resultant impacts on polar processes as detailed in Chapter 5 (see also Santee et al., 2024; Wohltmann et al., 2024).

In the Northern Hemisphere, Hunga water vapour reached the edge of the 2022/2023 Arctic vortex in the mid-stratosphere by January 2023, after it had de-

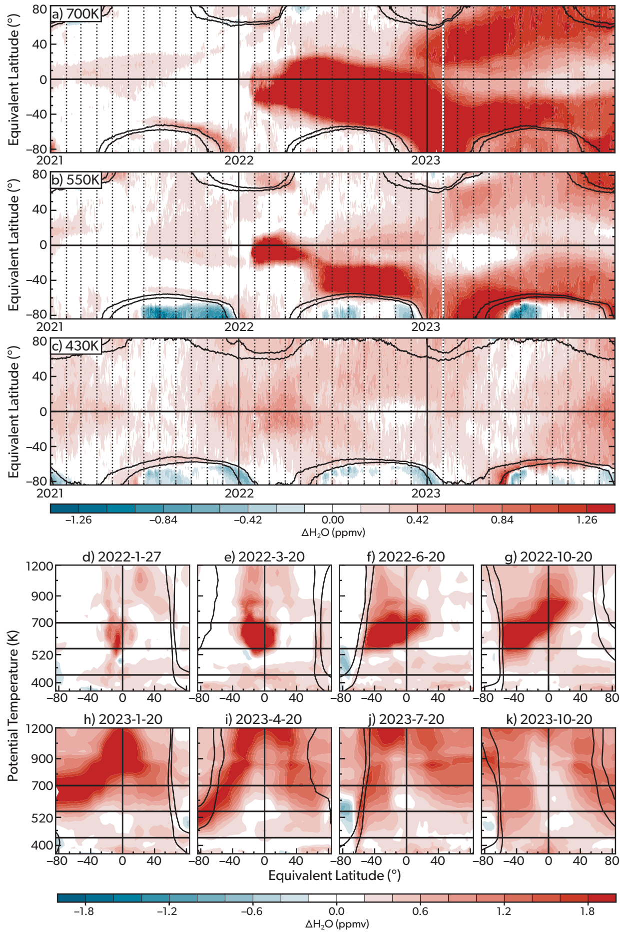

***Figure 3.8:*** *Time series and equivalent-latitude cross-sections of water vapour anomalies from MLS. (a–c) Time series of water vapour anomalies as a function of equivalent latitude for 2021–2023 at (a) 700 K (near 27 km, 18 hPa), (b) 550 K (near 23 km, 38 hPa), and (c) 430 K (near 18 km, 82 hPa). (d–k) Equivalent-latitude / potential-temperature snapshots of water vapour anomalies on eight representative days spanning 2022–2023. Black overlays on all panels are scaled potential-vorticity contours representing the vortex-edge region. Updated from Manney et al. (2023).*

veloped and presented a substantial transport barrier (Figures 3.8a, 3.8h); in the lower stratosphere near 20 km (Figure 3.8b) enhanced extra-vortex water vapour is seen outside the vortex starting in February, having descended from higher levels (Figures 3.8h, 3.8i). This enhanced water vapour was blocked from entering the vortex region until a mid-February sudden stratospheric warming resulted in extensive mixing between vortex and extra-vortex air, mixing high water vapour that had descended in the vortex from the upper stratosphere with high water vapour transported into the region from the Hunga plume (Lee et al., 2024). As in the SH, by the second fall after the eruption, Hunga-enhanced water vapour pervaded mid-latitudes and was entrained into the vortex as it developed. The 2023/2024 Arctic winter was characterised by two major sudden stratospheric warming events; the resultant lower stratospheric temperatures increases and associated transport resulted in much less than typical chemical ozone loss in Arctic spring 2024 (Newman et al., 2024).

### *3.3.2 Aerosol*

While the satellite measurements of aerosol extinction are not made in the polar night regions, the aerosol backscatter and depolarisation by CALIPSO CALIOP satellite lidar as well as by a ground-based cloud/aerosol lidar at Dumont d'Urville (DDU) station at 67° S can be used to study the transport of Hunga sulfate aerosols into the Antarctic region. In order to distinguish between solid polar stratospheric cloud (PSC) particles (NAT and ice) from liquid spherical particles (including PSC supercooled ternary solution, STS), we use CALIOP depolarisation ratio, providing information on the particle sphericity. In addition, we use 195 K as an approximate PSC-permitting temperature threshold (Peter, 1997) to identify the measurements unaffected by PSCs of any type.

Figure 3.9a displays the time-altitude series of scattering ratio restricted to liquid spherical aerosols (volume depolarisation below 5%; Pitts et al., 2018), which include volcanic sulfates and STS particles, from DDU lidar and CALIOP observations. While the first detection of a weak aerosol layer from Hunga over DDU was in mid-February 2022 (Khaykin et al., 2022), more substantial sulfate aerosol layers between 12-22 km altitude were observed throughout April 2022 (labelled T1 in Figure 3.9a) and afterwards between 18-23 km in mid-May (T2), just before the onset of the Antarctic polar vortex in June 2022 (grey shading in Figure 3.9a). The presence of Hunga sulfates in the southern high-latitude stratosphere by the time of vortex onset implies that the aerosols were most likely entrained by the vortex, however a reliable distinction between sulfate aerosols and subtle STS clouds that have similar optical properties is difficult using lidar observations. That said, the Hunga sulfates were present in the lowermost high-latitude stratosphere during the 2022 vortex season as suggested by the enhanced scattering ratio between 11-14 km outside the PSC-permitting temperature conditions represented by 195 K temperature isoline derived from DDU radiosoundings (white contour in Figure 3.9a).

A series of stronger enhancements in scattering ratio

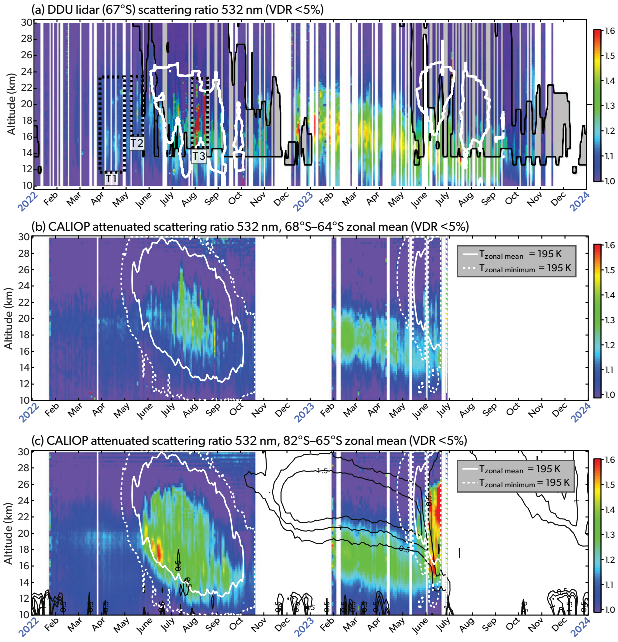

*Figure 3.9: Transport of Hunga sulfate aerosols into the Antarctic region from lidar observations. (a) Height-resolved time series of scattering ratio at 532 nm from ground-based lidar at Dumont d'Urville station (66.7° S, 140.0° E). Analysis is restricted to data with volume depolarisation ratio (VDR) < 5%, corresponding to spherical aerosols (sulfates and liquid PSC particles). Grey shading represents the polar-vortex mask defined using MERRA-2 reanalysis and the method of Lawrence et al. (2018). The white contour shows the 195 K temperature isoline (approximate PSC-formation threshold) from daily radiosoundings at DDU (minimum over a 7-day window). Black dashed rectangles labelled T1–T3 indicate the time/altitude windows referred to in the text. (b) Same as (a), but from CALIOP night-time zonally averaged measurements within the 68° S–64° S latitude band, without the vortex mask. Solid and dashed white contours indicate the 195 K temperature isoline (zonal mean and zonal minimum) from MERRA-2 data. (c) Same as (b), but for 82° S–65° S; black contours show MLS water-vapour anomalies in ppmv.*

between 14–22 km altitude during August 2022 (T3) can be attributed to STS clouds forming within the colder upper layer of the stratosphere. The locally observed time–altitude evolution of the scattering ratio from liquid aerosols is consistent with the zonal-mean CALIOP data at DDU latitudes (Figure 3.9b). After the final breakdown of the 2022 vortex, the excess aerosols from Southern-Hemisphere mid-latitudes expanded rapidly into high latitudes while slowly sedimenting. During the 2023 vortex season, the enhanced scattering ratios were observed mostly within the 10–15 km altitude layer outside the STS-permitting temperature environment (Figure 3.9a), and can thus be attributed to Hunga sulfates.

A broader perspective on the evolution of Hunga sulfates and liquid PSCs over the southern polar cap is provided by CALIOP zonal-mean observations between 82° S and 65° S (Figure 3.9c). During the 2022 Antarctic vortex, the time–altitude pattern of scattering ratio represented a typical signal of liquid PSCs (Tritscher et al., 2021), consistent with the 195 K temperature isoline. By the onset of the 2023 vortex, the Hunga sulfate aerosols were ubiquitous within the 14–18 km layer above the southern polar cap. At the same time, the MLS water vapour anomaly exceeding 0.5 ppmv was located at higher altitudes (black contours in Figure 3.9c), mostly above the aerosol layer. While both water vapour and aerosol anomalies were gradually descending at high southern latitudes, they entered the 2023 vortex at different levels, one above another. The aerosols entered the lower part of the vortex whereas the moist anomaly above 2.5 ppmv was entrained by the vortex in a wide altitude range between 19-26 km. This was immediately followed by a vortex-wide outbreak of liquid STS-type PSCs, which can be attributed to the excess of moisture. Indeed, a change in water vapour by 1 ppmv increases the threshold temperature for STS formation by about 1 K (Wohltmann et al., 2024). Another in-vortex layer of enhanced scattering ratio can be observed in early June at lower levels (15-17 km), vertically matching the aerosol layer entrainment by the vortex. It is conceivable that the pre-existing volcanic sulfate particles may also have enhanced the formation of STS clouds in the lower part of the 2023 vortex.

In addition to the lidar observations, several balloon-borne POPS soundings have been carried out from polar locations since the onset of the Hunga eruption. The unique microphysical signature of the Hunga aerosol particle size can trace the Hunga influence at polar latitudes. As shown in Figure 3.10a, at the northern high latitude station Utqiaġvik (Alaska, 71° N) in March 2023, the effective radius profiles in the stratosphere above 10 km do not present large layers with a strong Hunga signature. Note that the two profiles on 14 and 15 March 2023, sampled the polar vortex and measured lower effective radii between 15-20 km in altitude. The profile of March 14 presents some effective radius enhancement above 0.2 µm that may be attributed to Hunga particle influence. This is consistent with a mixing between smaller size background aerosol and Hunga particles, as identified in lower latitudes in the northern hemisphere (Section 3.1).

Below 10 km, the variability is likely due to aerosol transport in the free-troposphere, often impacted by wildfires even early in the season.

In the southern high latitudes (Figures 3.10b–3.10c), data from Scott Base (78° S) and the South Pole Observatory (Amundsen–Scott Station, 90° S) there is no strong evidence of concentrated Hunga plume reaching Antarctica by November 2022 (Figure 3.10b). However, the effective radius peaks just above 0.2 µm between 10-15 km and may be due to mixing with Hunga particles. In Austral spring 2023, the Hunga aerosols are unambiguously present above Antarctica with effective radius reaching up to 0.36 µm above 10 km. At South Pole (Figure 3.10c), available profiles during the Austral winter and spring 2024 highlights a return to the state observed at Scott Base during the Austral spring 2023. These profiles exhibit the low effective radius signature of the polar vortex above 15 km. During Austral summer 2025 in South Pole, Hunga signature is not perceived.

## 3.4 Uncertainty of observations

### 3.4.1 Aerosol optical depth and extinction

Uncertainty in the aerosol extinction coefficients and optical depth obtained from satellite measurements is evaluated by comparing solar occultation observations from the SAGE III/ISS instrument with limb-scatter measurements from the OMPS-LP instrument. For the latter, results from three different retrieval algorithms—NASA, the University of Bremen (IUP), and the University of Saskatchewan (USask)—are analysed (Taha et al., 2021; Bourassa et al., 2023; Rozanov et al., 2024). As those three retrievals use the same measured radiances, the resulting differences in retrieved extinction illustrate the influence of different assumptions about, e.g., aerosol particle size distribution and different retrieval techniques. In addition, results obtained from measurements of the limb-scatter OSIRIS instrument are shown. OSIRIS is in a different orbit than OMPS-LP, thus the differences between the results from those retrievals are also due to the viewing geometry, i.e. different single scattering angles, and illustrate the influence of the assumption about the aerosol particle size distribution. Dependence of the retrieval results on the assumption about the particle size distribution and viewing geometry is discussed e.g. by Rieger et al. (2019).

Figure 3.11 shows the time series of aerosol optical depth from SAGE III/ISS, OSIRIS, and all three available OMPS-LP retrievals in three latitude bands in the Southern Hemisphere. The dots show individual measurements while the solid curves are a 60-day rolling average to account for sampling gaps. In the time period with relatively weak volcanic activity before 2022, results from all satellite instruments and different retrievals agree very well in terms of the magnitude and temporal variation. The only exception is the first half of 2020 in the 50°–40° S latitude band, where the aerosol load of the stratosphere was strongly influenced by the Australian bush fires. For this period SAGE III/ISS results are on the upper range and USask OMPS-LP data are on the lower range of the spread. The differences between the minimum and maximum values reach about 50% in the beginning of 2020.

In contrast to the limb-scatter observations made by OMPS-LP and OSIRIS, SAGE III/ISS occultation measurements do not require any assumptions about aerosol type or particle size distribution to derive extinction. For this reason, SAGE III/ISS results are considered most reliable when considering single retrievals. Some issues might however arise for monthly mean data because of a sparsity of spatio-temporal sampling of the solar occultation measurements. After the Hunga eruption in January 2022, the spread between different data sets drastically increased. The NASA results are generally at the upper edge of the spread while OSIRIS values are always significantly lower in comparison to all others. OMPS-LP retrievals from IUP and USask are typically close to each other and systematically lower than SAGE III/ISS results. OMPS-LP results of NASA are typically higher than those from SAGE III/ISS. Despite the differences in the absolute values of the aerosol extinction, the shape of the extinction peak in the first half of 2022 is similar for SAGE III/ISS and all OMPS-LP retrievals. Larger differences in the temporal variation of the aerosol depth are seen in 2023. In the 50°–40° S latitude band, the second peak in the optical depth is observed in OMPS-LP NASA earlier than in the SAGE III/ISS results while OMPS-LP retrievals from IUP and USask do not show any secondary peak at all. In the 30°–20° S latitude band, the secondary peak is quite strong in OMPS-LP NASA results, much weaker in OMPS-LP USask time series and is not seen in SAGE III/ISS and OMPS-LP IUP data. In the 10° S–10° N latitude band, SAGE III/ISS and OMPS-LP IUP agree reasonably well, while OMPS-LP retrievals from NASA and USask show secondary peaks later in 2023. In 2024, the stratospheric aerosol load decreases toward the pre-eruption level and the agreement between different data sets significantly improves.

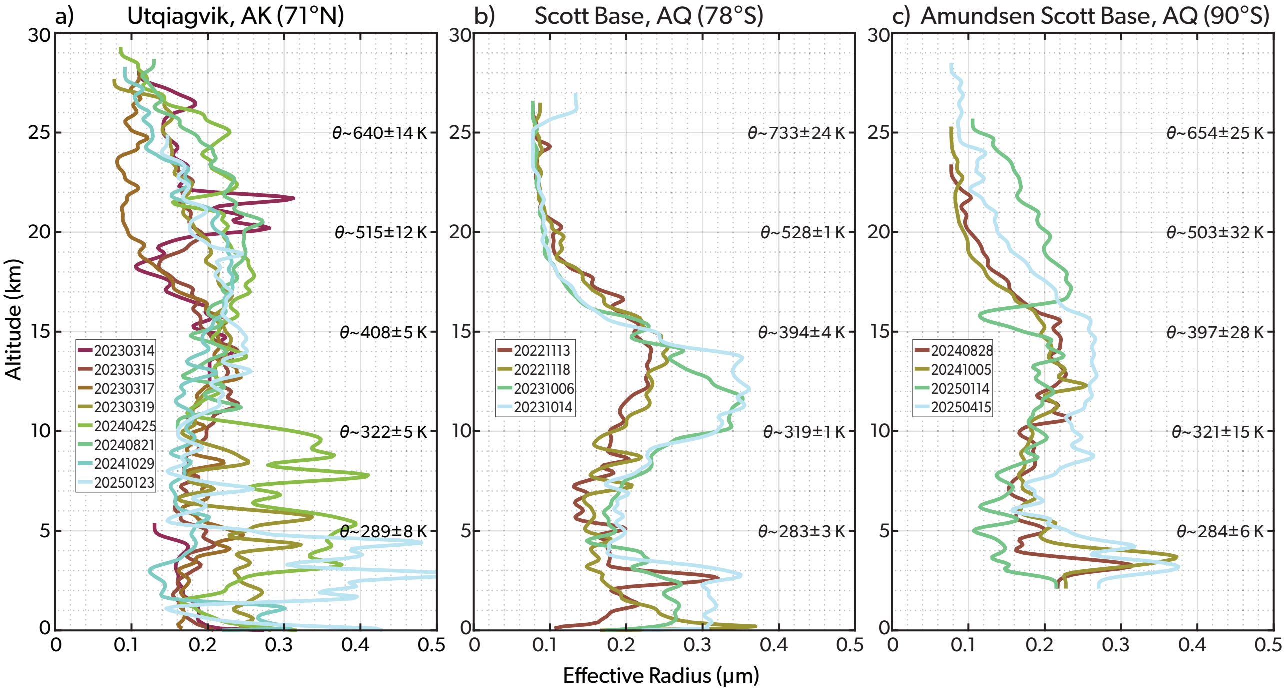

***Figure 3.10:*** *Aerosol effective radius derived from balloon sounding measurements (radius range 0.07–1.25 μm) at polar stations: (a) Utqiaġvik (71° N), (b) Scott Base (78° S), and (c) South Pole (90° S). Potential-temperature equivalent levels averaged over the plotted profiles are displayed on the right axis of each panel.*

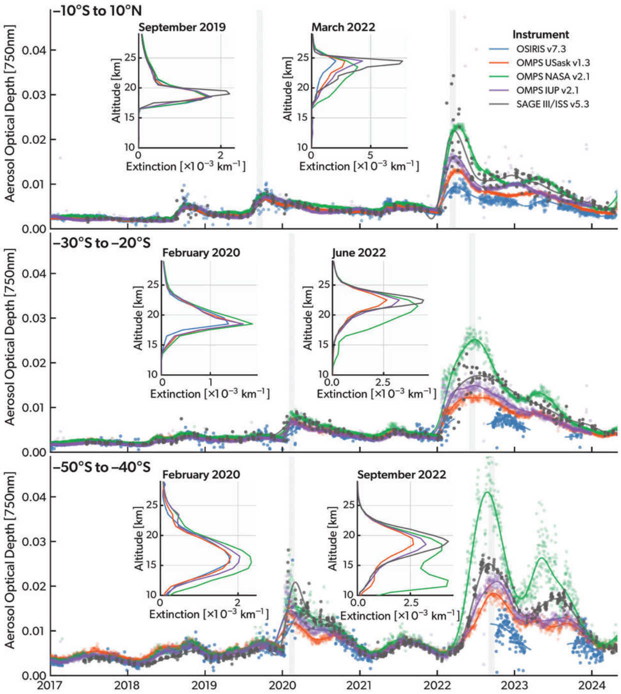

***Figure 3.11:*** *Time series of aerosol optical depth from SAGE III/ISS, OSIRIS, and all three OMPS-LP retrievals (NASA, IUP, and USask) in three latitude bands of the Southern Hemisphere. Inset panels show the monthly mean extinction profiles from each instrument for the months marked by vertical grey shaded regions.*

A strong factor for the differences observed after the Hunga-Tonga eruption is likely the assumption of the aerosol particle size distribution needed for the limb-scatter retrieval algorithms for the radiative transfer forward model. The results indicate that a particle size distribution typical for the background aerosol conditions, which is assumed in the limb-scatter retrievals, is not adequate for the atmospheric conditions after the Hunga-Tonga eruption and adds substantial uncertainty to these data sets.

The inset panels in Figure 3.11 show the monthly average extinction profiles from each instrument for months marked by the vertical grey shaded regions. From these plots we see that for weak perturbations in the stratospheric aerosol as seen e.g. in February 2020 in the 30°–20° S latitude band and in September 2019 in the 10° S–10° N latitude band, results from all instruments agree reasonably well. For a stronger perturbation as seen in March 2020 in the 50°–40° Slatitude band, larger differences are observed. NASA results show the best agreement with SAGE III/ISS while the OSIRIS data are the lowest and show higher peak altitude as compared to all other data sets. Within the Hunga aerosol, OMPS-LP retrievals from IUP and USask agree very well with SAGE III/ISS data in terms of the profile shape and peak altitude but show significantly lower values in the peak range. The OMPS

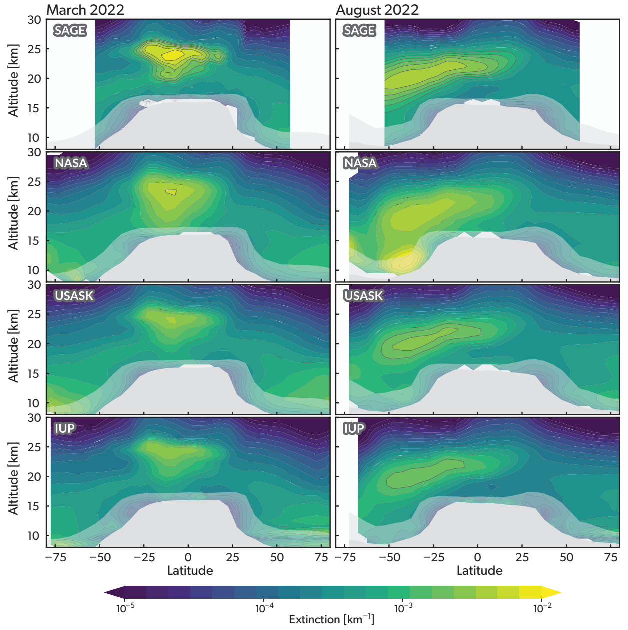

***Figure 3.12:*** *Comparison of aerosol extinction at 750 nm from all three OMPS-LP retrievals and SAGE III/ISS. Panels show zonal averages from each instrument for March (left) and August (right) 2022. The light-grey region indicates altitudes that are sometimes in the stratosphere; the opaque grey region indicates altitudes always in the troposphere.*

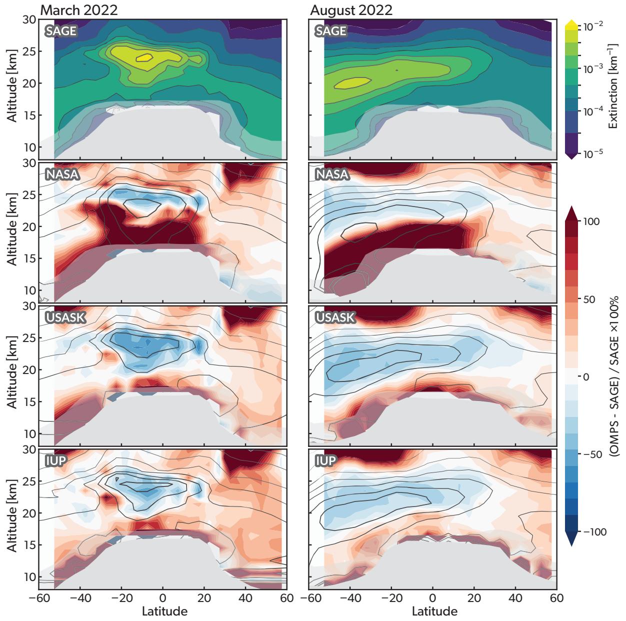

***Figure 3.13:*** *Comparison of aerosol extinction at 750 nm from all three OMPS-LP retrievals and SAGE III/ISS. Panels show zonal averages from each instrument and the corresponding percent difference of OMPS-LP from SAGE III/ISS. Black contours show the extinction from each instrument, delineating the region of the Hunga aerosol. Light-grey regions indicate altitudes that are sometimes in the stratosphere; opaque-grey regions indicate altitudes always in the troposphere.*

NASA retrieval shows similar peak values as SAGE III/ISS (except for March 2022 in the 10° S–10° N latitude band) but somewhat lower peak altitude and very different profile shape. The aerosol extinction coefficient values below the profile peak reported by the NASA retrieval are much higher compared to all other data sets.

The high bias of the NASA retrieval below the profile peak seen in example plots in Figure 3.11 is also clearly illustrated in Figure 3.12, which shows the aerosol extinction profiles from SAGE III/ISS and three OMPS-LP retrievals for two example months (March 2022 in the left panel and August 2022 in the right panel) as a function of the altitude and longitude. This plot is done using the zonal monthly mean data for all instruments and retrievals. Figure 3.12 shows that the OMPS-LP IUP and USask retrievals reproduce the shape of the aerosol plume seen by SAGE III/ISS very well but show consistently lower values. In the OMPS-LP NASA results the shape of the aerosol plume is distorted below the peak and the resulting aerosol extinction coefficients are often higher than those from SAGE III/ISS.

The relative differences with respect to the SAGE III/ISS data for all three OMPS-LP retrievals in March and August 2022 are shown in Figure 3.13. The position of the Hunga-Tonga aerosol plume is shown by the overlaid black contours. The shape of the differences is very similar for IUP and USask retrievals with a low bias in the aerosol plume peak area and high bias outside. The differences are larger in March 2022 (within 2 months after the eruption) reaching about 60% for USask and 40% for IUP retrievals. The differences for the OMPS-LP NASA retrieval show a pronounced vertical structure around the peak altitude with a low bias of up to about 50% above the peak altitude and a positive bias exceeding 100% below. In the Northern mid-latitudes, where only occasional penetrations of the Hunga-Tonga aerosols were observed, the pattern of the differences with respect to SAGE III/ISS results is similar for all three OMPS-LP retrievals but the absolute values of the differences are somewhat higher for OMPS-IUP retrieval. Comparisons poleward of 60°N/S are not always possible due to the more limited latitudinal coverage of SAGE III/ISS compared to OMPS-LP. The feasibility of extending GloSSAC with the OMPS measurements to help fill these gaps is currently under investigation (Kovilakam et al., 2025).

The results discussed in this section show that the

(a) MLS $H_2O$ mass perturbation, 19 km–60 km

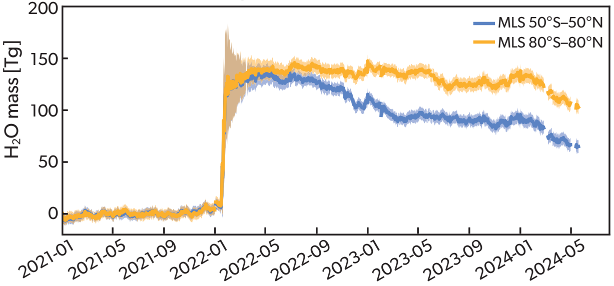

(b) $H_2O$ mass perturbation, 50°S–50°N, 19 km–60 km

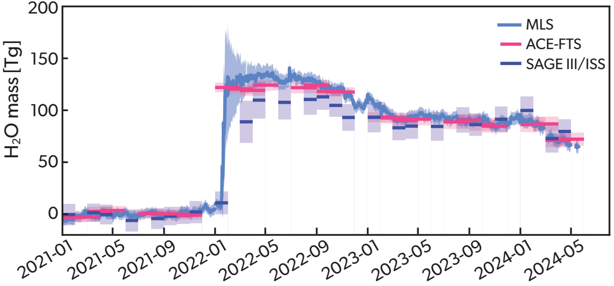

***Figure 3.14:*** *Stratospheric water-vapour mass anomaly from MLS, ACE, and SAGE III/ISS. Daily averages are shown for MLS, whereas the coarser sampling from occultation instruments (ACE and SAGE) requires 2–3-month averages to capture the latitudinal distribution.*

results from SAGE III/ISS and different OMPS-LP retrievals agree well for background aerosol conditions. After the Hunga eruption, the spatio-temporal evolution of the volcanic plume is essentially captured by all satellite data sets considered here, but large differences occur in the magnitude of the aerosol extinction. The size of the differences depends on the retrieval and on the time after the eruption. This confirms previous findings, that a realistic assumption about the aerosol particle size distribution is important for limb-scatter retrievals (Rieger et al., 2014), and that strong volcanically perturbed particle size drives large uncertainty in these observations.

### 3.4.2 Water vapour

The uncertainty in the water vapour observations can also be investigated through comparison of satellite observations. Like the aerosol, the water vapour levels are substantially different from those ever encountered before in the era of space-borne observations posing potential issues for the available measurement and retrieval approaches. There are three main satellite instruments that are able to measure water vapour profiles in the stratosphere with reasonable vertical resolution and coverage across a wide range of latitudes: MLS, ACE-FTS, and SAGE III/ISS. While these are all limb sounding instruments, the measurement approaches of these three instruments are quite different in terms of spectral range and sampling. MLS measures emitted radiation from the atmosphere in the microwave spectral region, while ACE-FTS and SAGE III/ISS measure attenuated solar radiation through occultation with ACE-FTS observing in the mid-infrared, and SAGE III/ISS in the visible and near infrared.

MLS has by far the best global coverage of the three, with daily global coverage extending up to latitudes greater than 80° latitude. Figure 3.14a shows the daily zonal average time series of water vapour mass anomaly as measured by MLS for latitudes 80°S to 80°N and altitudes between 19-60 km. Note that this is essentially the same as the global percent anomaly shown in Figure 3.1d; however, here mass units are calculated following the methodology in Khaykin et al. (2022). Also, the MLS data are first corrected for the artefact reported by Millán et al. (2024), which is caused by a discontinuity in the retrieval *a priori* following the methodology suggested in that paper.

Figure 3.14a also shows the same water vapour mass anomaly but for a reduced latitude range of 50°S-50°N to facilitate the comparison with the SAGE III/ISS and AGE-FTS solar occultation observations, shown in Figure 3.14b. The reduced sampling of the solar occultation technique means it requires 1-2 months to sample the latitudinal extent enabled by the orbit, and that the highest latitudes are sampled more infrequently. One month time averages for SAGE III/ISS and 2 month time averages for ACE-FTS limited to latitudes 50°S-5°N provide a good balance between number of samples and latitudinal coverage. Even at this resolution, some bins do not cover the full range of latitudes, and bins that are not fully sampled at least every 10 degrees are removed from the analysis and left as a gap in the time series. Water vapour mass anomaly is then calculated using the same approach as for MLS with minor adjustments to handle the altitude rather than pressure level coordinates of the occultation data sets.

It is clear from Figure 3.14b that the agreement between all three measurement sets is highly robust. Aside from the first 6 months after the eruption where the atmospheric variability is quite high (as seen in the standard deviation of the measurements shown with shaded colours) the three instruments agree within about 10 Tg, which is less than 10% of the total mass anomaly. Even the decay observed in the water vapour mass starting in early 2024 is very well captured by all three data sets. SAGE III/ISS has an unexplained but small low bias compared to ACE-FTS and MLS during approximately the first year after the eruption that is gradually rectified in early 2023. ACE-FTS and MLS agree extremely well with each other throughout the time series, even during the first few highly variable months after the eruption.

## 3.5 Modelling of the Hunga plume evolution

The objective of this section is to evaluate the fidelity of the simulated medium-term (1 month – 2 years) evolution of sulfate aerosol and water vapour in seven global climate models: CAM5/CARMA, WACCM6/CARMA, MIROC-CHASER, GEOSCCM, GEOS/CARMA, LMDZ6.2-LR, and WACCM6/MAM. Model skill in simulating volcanic aerosols and their impacts is typically assessed for sulfur-rich eruptions such as Mt. Pinatubo. The uniqueness of the Hunga–Tonga eruption, however, provides an unprecedented opportunity to test models under conditions markedly different from those for which they were originally developed, thereby enhancing confidence in their ability to simulate future eruptions.

In each of the subsections below, the key features of the observations are briefly summarised, followed by an evaluation of those features in the models. While the mechanisms responsible for the differences between the various models are of scientific interest, an investigation of the causes of the model differences is beyond the scope of this report. Studies examining the differences in the simulated plume evolution, the longer-term evolution of the Hunga perturbations in free-running ensemble simulations (Zhuo et al., 2025), and the radiative forcing estimates in the various models (Quaglia et al., 2025) are submitted or in preparation at the time of writing this report. These efforts augment the Tonga Model Intercomparison Project (Tonga-MIP) focused on the first three months after the eruption (Clyne et al., 2024).

The simulated global transport and evolution of Hunga materials are evaluated through analysis of *Experiment 2a* of the HTHH-MOC project (Zhu et al., 2025) (see also Supplementary S1 and S3, Part 1).

In these simulations, temperatures and/or winds are nudged to a reanalysis product to evaluate the model representation of the volcanic eruption without interannual variability. For each model, the magnitude and altitude of the injection of water vapour are chosen with the goal to retain 150 Tg of water at the MLS-observed altitude one week after the eruption. All models inject 0.5 Tg of $SO_2$, but the injection location is not required to be co-located with the water vapour injection. Experiment 2a models all include a prognostic aerosol module but vary in the complexity of their representation of aerosol microphysics (i.e., bulk, modal, or sectional). Detailed model descriptions and specifications for the simulations are found in Zhu et al. (2025).

### *3.5.1 Meridional dispersion of the volcanic aerosol and water vapour*

The evolution of the sulfate aerosol and water vapour anomalies as observed by satellites (Section 3.1) suggests distinct transport pathways and episodic events. Observations of SAOD indicate the meridional dispersion of sulfate aerosols in the southern tropics within two months of the eruption, followed by a more efficient winter transport from the tropics towards the southern extratropics by June 2022 (Figures 3.1a and 3.15a). Northward cross-equatorial transport was relatively weak and sporadic, but enhanced SAOD was clearly observed as far north as 20°N within three months after eruption. After several episodic in-mixing events, the aerosols reached the northern extratropics by early 2023.

The observed aerosol transport is well simulated by all models (Figure 3.15). Most models simulate the transport from the tropics to the southern midlatitudes by June-July 2022 and to the southern high-latitudes by the end of 2022. Overall, models underestimate the magnitude of the SAOD compared to observations, as visible in the comparisons with OMPS in Figure 3.15 and with GloSSAC in Figure 3.19 (see NASA/LARC/SD/ASDC, 2023), indicating that the prescribed 0.5 Tg of $SO_2$ might be insufficient to reproduce the magnitude of the stratospheric aerosol perturbation (see Chapter 7 for a discussion of this issue).

Most of the Hunga aerosols remain outside of the Antarctic vortex during the first year in all models, in agreement with observations. Note that SAOD is enhanced within the Antarctic vortex in many models (except MIROC-CHASER and LMDZ6.2-LR), but the aerosol burden is due to background aerosols in the respective models (Figure S3.1 shows the simulated background SAOD from a control run without the Hunga eruption, and Figure S3.2 shows the SAOD simulated anomaly with respect to the control run). All models except for MIROC-CHASER and LMDZ6.2-LT simulate the entrainment of aerosols into the Antarctic vortex of 2023.

While some cross-equatorial transport is evident in all models within the first few months after eruption,

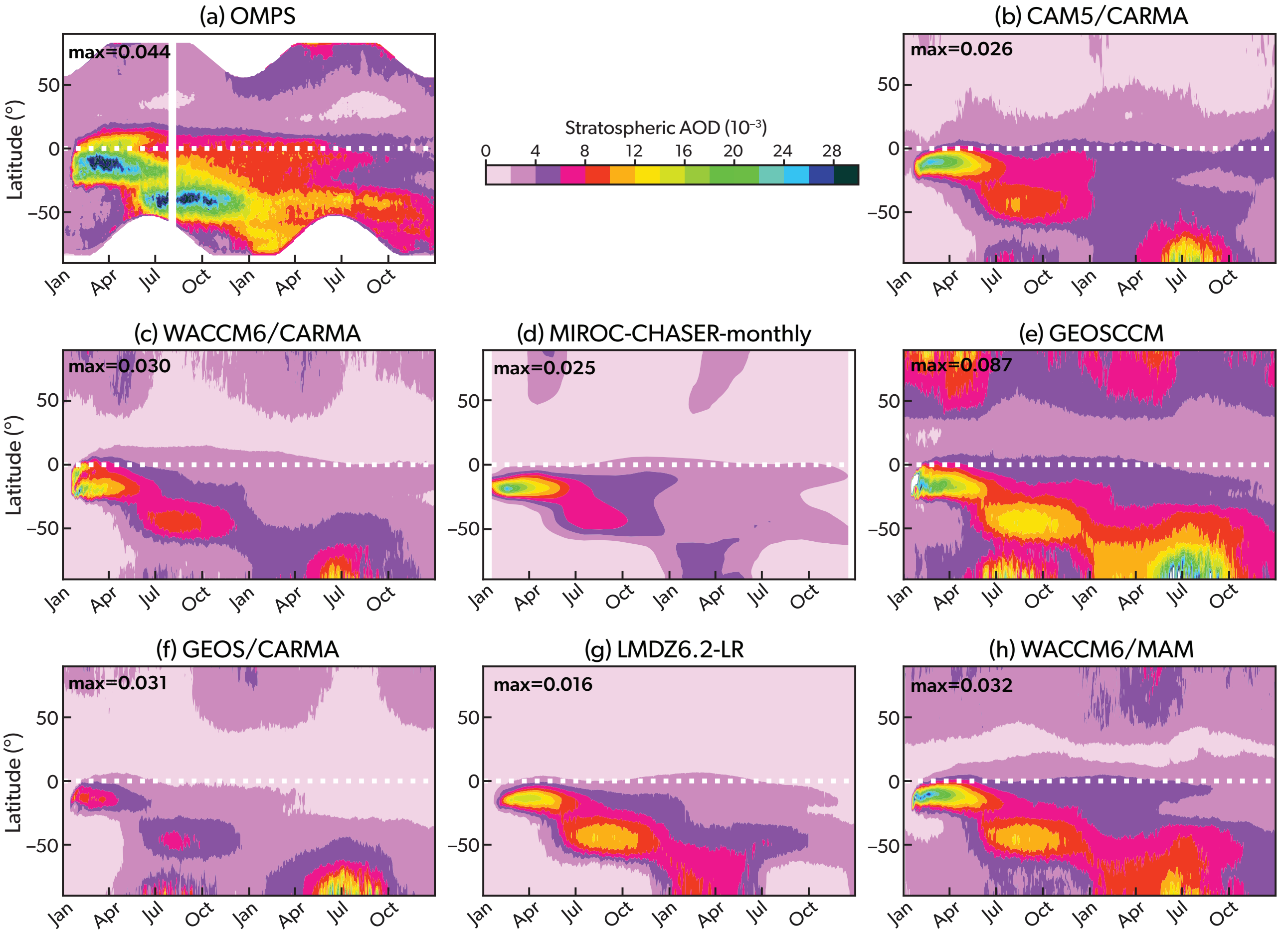

***Figure 3.15:*** *Meridional dispersion and evolution of Hunga aerosol in global models and observations from January 2022 to December 2023. Stratospheric aerosol optical depth (SAOD) is plotted as a function of time and latitude. All panels show near-infrared SAOD. SAOD values were calculated from daily data, except for MIROC-CHASER (d), which used monthly means.*

the fraction of SAOD in the NH is generally lower than in observations (Figure S3.3). The entrainment into the developing Arctic vortex is only simulated in GEOS/CARMA (Figure S3.2f).

The water vapour transport over the first year as observed by MLS was characterised by a large perturbation in the tropics (0–20° S) within two months of the eruption followed by transport into the southern midlatitudes in mid-June 2022 and into the northern extratropics in January 2023. After reaching the stratopause in early 2023, most of the Hunga water vapour was transported to the mid and high latitudes. Hunga's water vapour was not entrained into the Antarctic and Arctic vortices until the following year. To compare the water vapour transport pattern in each of the models with observations, the simulated SCWV were computed as density-weighted water vapour mass mixing ratios vertically integrated above 100 hPa. SCWV perturbations (g $m^{-2}$) were calculated with respect to the simulations without water vapour and sulfur dioxide injections from the eruption (Figure 3.16 shows perturbations; Figures S3.4 and S3.5 show absolute values of the stratospheric water vapour column).

The overall pattern of the water vapour transport during the first two years is reproduced well by the models (Figure 3.16). For example, all models simulate the meridional dispersion of water vapour from the tropics to the southern midlatitudes around June 2022 and the entrainment into the Antarctic vortex in late 2022. Despite the differences in the background SCWV between the models, the timing and magnitude of the simulated SCWV perturbations are roughly in agreement with MLS observations.

The major episode of northward water vapour transport in January 2023 is reproduced well in most models (northward transport is virtually absent in MIROC-CHASER and LMDZ6.2-LR). The smaller cross-equatorial transport event in March-April 2022 is also present in all models except for MIROC-

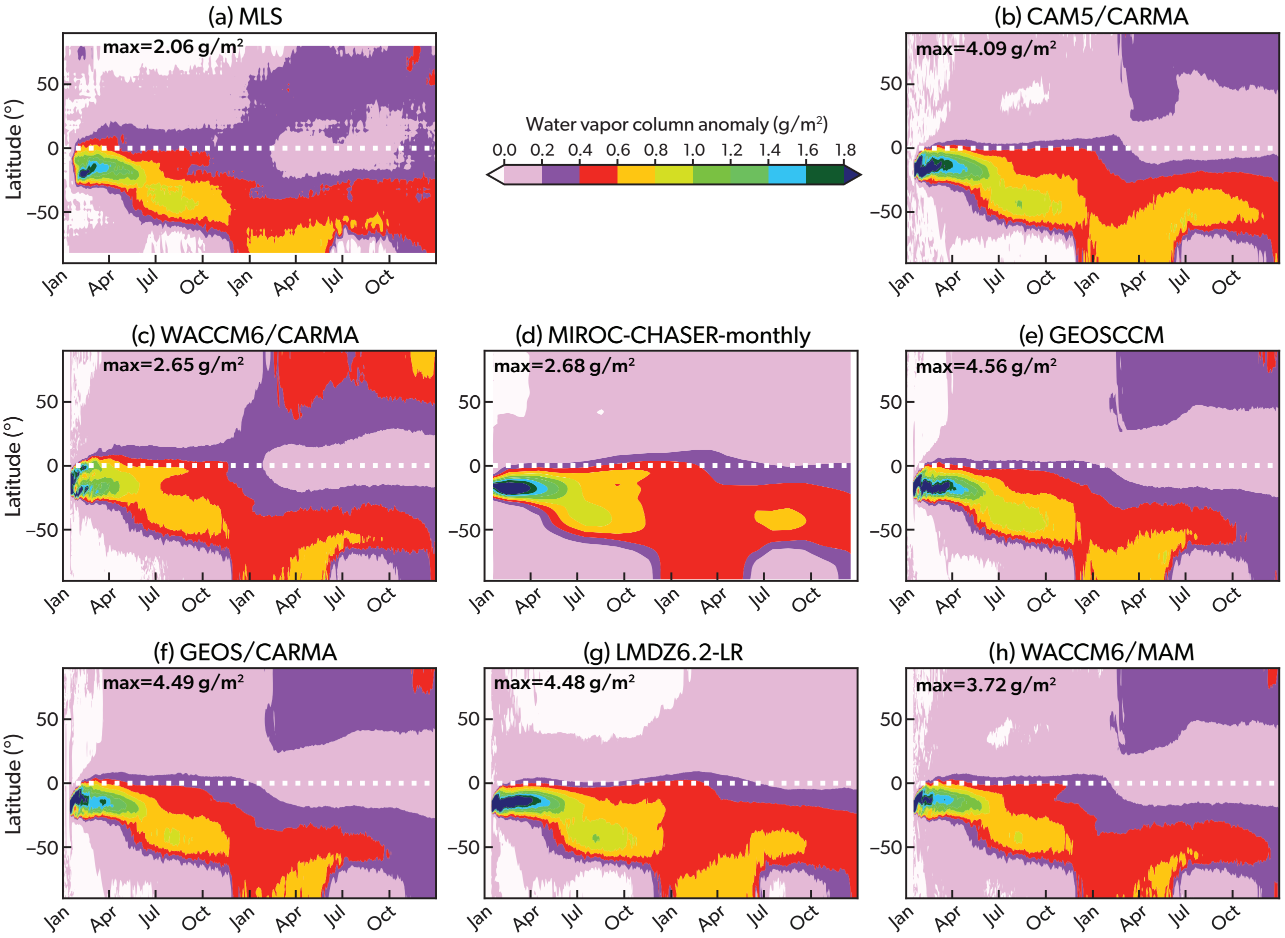

*Figure 3.16: Meridional dispersion and evolution of Hunga water-vapour perturbations in global models from January 2022 to December 2023. Perturbations are calculated relative to simulations without water-vapour and sulfur-dioxide injections, based on daily values except for MIROC-CHASER (d), which uses monthly means. Numbers in the upper left of each panel indicate the maximum anomalies reached. MLS water-vapour anomalies are calculated with respect to January 2022 using deseasonalised values for 2022–2024.*

CHASER but its latitudinal extent is underestimated. By spring 2023, most of the Hunga water vapour resides outside of the tropical belt, as in observations, except in MIROC-CHASER and LMDZ6.2-LR where moisture remains elevated in the southern tropics. The good overall agreement of the water vapour perturbations in CAM5/CARMA, WACCM6/CARMA, GEOSCCM and GEOS/CARMA with MLS observations suggests that the large-scale transport via the Brewer-Dobson circulation as well as the dynamics of the Arctic and Antarctic polar vortices are well represented in those models.

### 3.5.2 Vertical separation of the volcanic aerosol and water vapour and evolution of the aerosol radius

As noted in Section 3.1 and illustrated in Figure 3.2, the different meridional dispersion patterns of aerosols and water vapour starting in late 2022 are largely driven by the vertical separation of the aerosol and water vapour clouds. The water vapour began to rise through the mid stratosphere in October 2022 and subsequently experienced a steep rise in April 2023 associated with the rapid transport from the tropical pipe to northern high latitudes. After crossing the stratopause in early 2023, the bulk of the water vapour resided in the mesosphere by early 2024. Meanwhile, aerosols gradually descended towards the tropopause (Figure 3.3a and Figure S3.6).

All models show a vertical separation between the ascending water vapour and the descending aerosols in the tropics starting around late 2022 (Figure 3.17), in agreement with observations Figure 3.2a). The vertical separation in the models is primarily due to the gravitational settling of aerosol particles, which causes the aerosols to descend while water vapour ascends via the tropical upwelling branch of the Brewer-Dobson circulation (after the initial radiative cooling

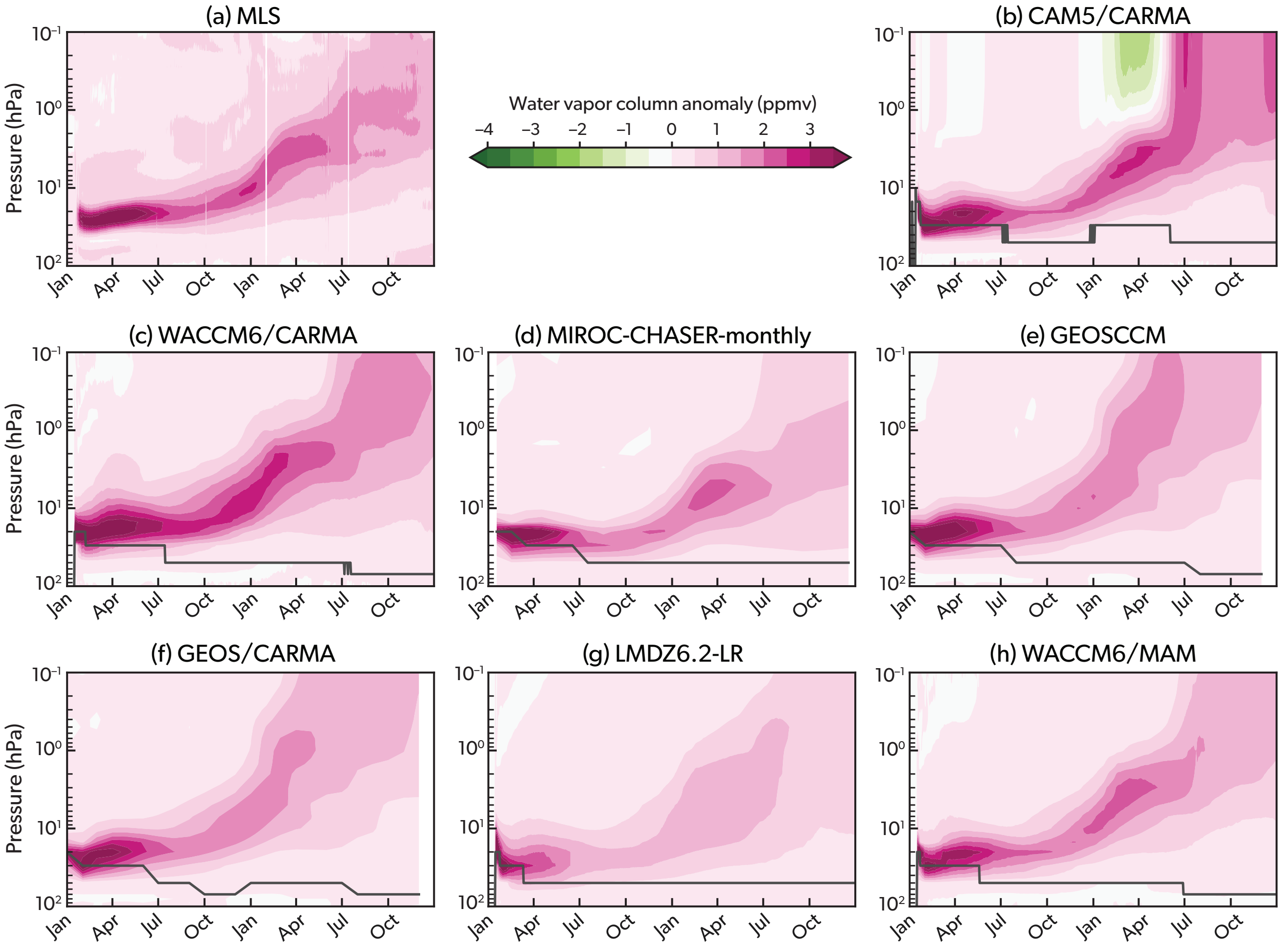

*Figure 3.17: Zonal-mean water-vapour perturbation (colour, in ppmv) as a function of time and altitude, averaged over 30° S–30° N in global models from January 2022 to December 2023. The black line shows the altitude of the maximum aerosol extinction coefficient (or mass-mixing ratio for CAM5/CARMA) above 100 hPa. Corresponding observations are shown in Figure 3.2a. Perturbations are based on daily values except for MIROC-CHASER, GEOSCCM, and GEOS/CARMA, which use monthly means.*

until October 2022). The simulated rate of tropical upwelling agrees well with observations in most models, with the Hunga moisture reaching the 1 hPa level by early 2023. Most models also simulate the steep rise of the Hunga water vapour into the mesosphere in April 2023. When compared to observations, the tropical ascent is too fast in GEOSCCM and too slow in MIROC-CHASER. Water vapour perturbations in CAM5/CARMA ascend slowly until just below the stratopause and are capped by negative water vapour perturbations in the mesosphere in early 2023. The very rapid ascent into the mesosphere in mid 2023 is much too fast compared to MLS observations. Overall, the timing and altitude of the appearances of the water vapour perturbations are simulated reasonably well in all models. The altitude of the sulfate aerosols (shown by the black line in Figure 3.17, and shown more clearly in Figures S3.6 and S3.7) is similar in all models and centered between 50 and 30 hPa (~25 km).

All of the models considered here, except for GEOSCCM, contain a parameterisation of aerosol microphysics and simulate the evolution of the particle radii (Figure 3.18 in the tropics and Figure S3.8 in the extratropics). CAM5/CARMA, WACCM6/CARMA, GEOS/CARMA, and LMDZ6/2-LR use a sectional aerosol microphysical model, while MIROC-CHASER, and WACCM6/MAM use two different versions of the MAM modal model. In all models, the effective radius grows quickly after the eruption and equilibrates between 0.2 and 0.3 $\mu$m after the larger particles settle out of the stratosphere. The increase in effective radius due to the eruption varies across models and is generally up to 2.5 times larger than the background (Figure S3.9). LMDZ6.2-LR simulates a slower growth in particle size and peaks at a much smaller radius than the other models, probably because the aerosol burden in this model is much smaller than in the others. Two years after the eruption, all models still

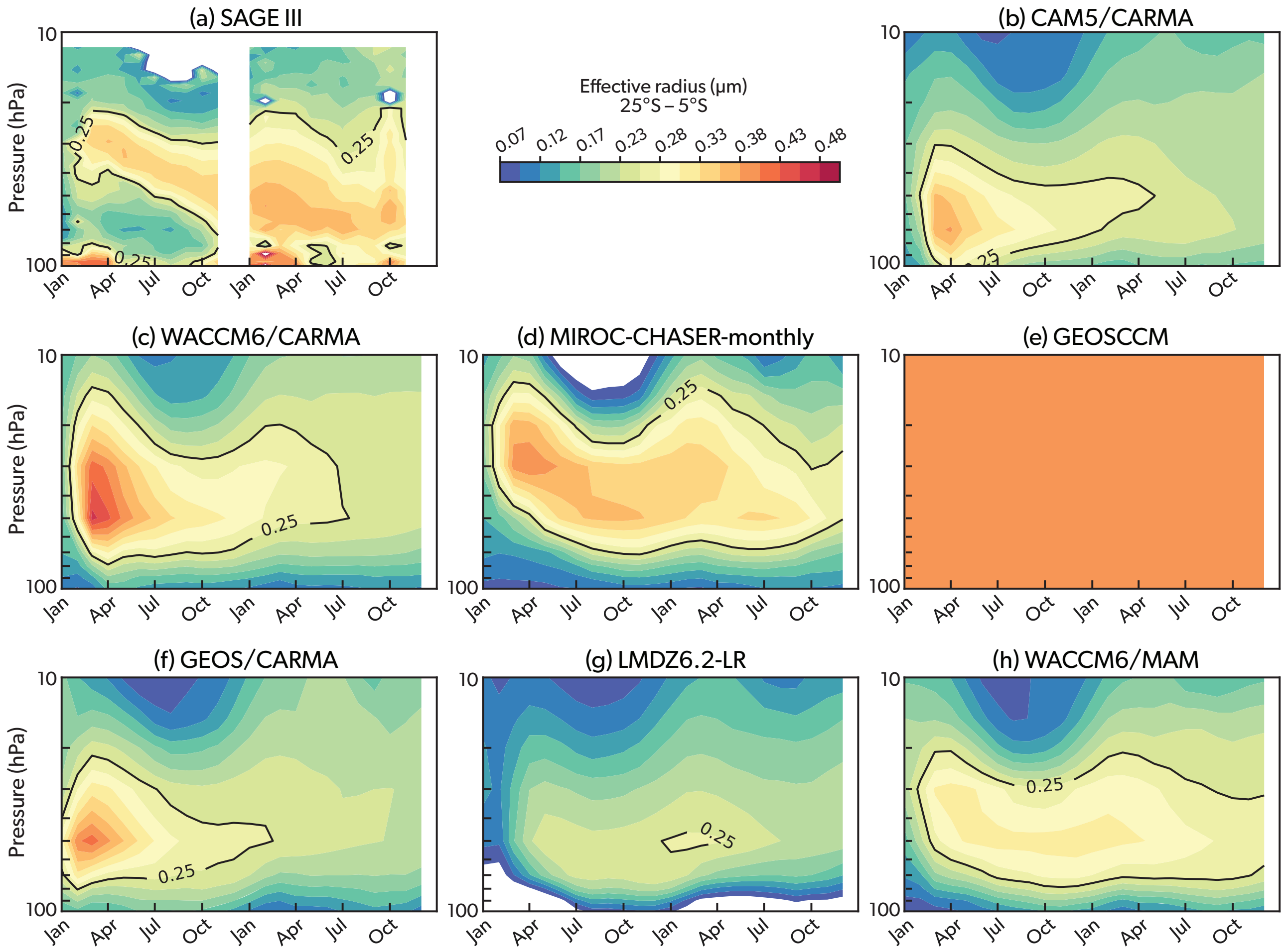

**Figure 3.18:** *Monthly mean aerosol effective radius averaged over the southern-hemisphere tropics (5° S–25° S) as a function of time and altitude in SAGE III/ISS and in different models from January 2022 to December 2023. GEOSCCM is a bulk model and assumes a constant effective radius of 0.4 μm.*

simulate particles size larger than the background.

### 3.5.3 Longevity and decay of the water-vapour and aerosol perturbations

The GloSSAC V2.21 merged satellite data set shows that the near global (60° S–60° N) SAOD anomaly grows rapidly after the eruptions reaching a maximum of approximately 0.006 in July-August 2022, followed by a decay phase (Figure 3.19). By the end of 2024, GloSSAC still records elevated SAOD with respect to the 2013 values, which we consider background conditions.

The simulated global mean SAOD perturbations reach a maximum soon after eruption and enter the decay phase in each of the models (Figure 3.19). Except for LMDZ6.2-LR and GEOS/CARMA, the initial enhancement in near-global SAOD occurs earlier than observed. This suggests that either the aerosol formation is too fast in most models, or that the observations underestimate the early peak in SAOD because

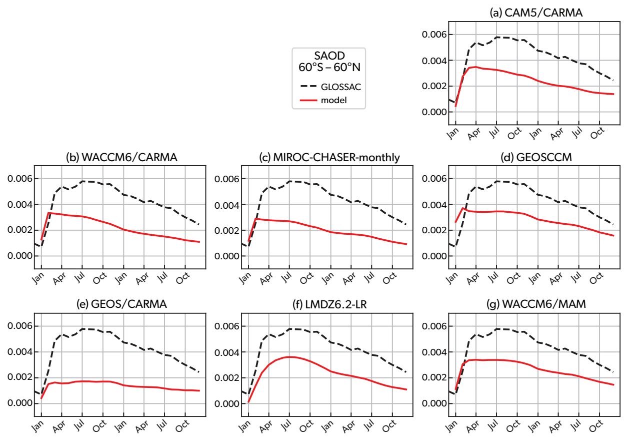

**Figure 3.19:** *Time series of monthly mean near-infrared (near-IR) stratospheric aerosol optical depth (SAOD) anomalies averaged over 60° S–60° N in the GloSSAC dataset (Thomason et al., 2018) (black dashed line) and in models (red solid lines) from January 2022 to December 2023. The GloSSAC anomalies are calculated relative to 2013, while the model perturbations are relative to simulations without the Hunga eruption.*

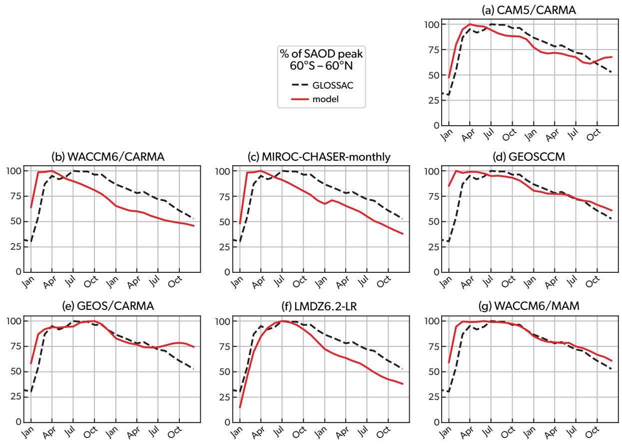

**Figure 3.20:** *Fraction (in %) of monthly mean near-IR SAOD with respect to its maximum, averaged over 60°S–60°N, in the GloSSAC dataset (black dashed line) and in models (red lines).*

of sampling. While all models underestimate the magnitude of SAOD compared to observations, the decay rate of the global SAOD is remarkably well simulated compared to the GloSSAC dataset (Figure 3.20).

Several factors may have contributed to the lower SAOD values in the models compared to observations, primarily pointing to a too low injection of sulfur dioxide. Another likely explanation is that the simulated conversion to sulfate aerosol may have been too fast, leading to too large particles (Figure 3.18) that sediment quicker than in observations and with a lower extinction efficiency.

The Hunga eruption increased the global SCWV by more than 15% for a period of about two years (Figures 3.1c,d). The increase was most dramatic in the SH reaching 24% of climatological mean value shortly after eruption. The cross-equatorial transport to the NH in Mar-Apr 2022 decreased the SH burden to about 22% and increased the NH burden to about 11%. By March 2023, hemispheric SCWV perturbations converged with the global perturbation of about 15% and stayed at roughly the same level throughout the following year.

The time series of the global simulated SCWV perturbations show a rapid increase after the Hunga eruption of a magnitude similar to observations in all models (Figure 3.21). CAM5/CARMA, MIROC-CHASER, GEOSCCM, and LMDZ6.2-LR models simulate the correct magnitude and timing of the global and southern hemispheric perturbations, while they underestimate the perturbation in the northern hemisphere. This suggests that the meridional dispersion of the water vapour plume is underestimated in these models, which is confirmed in Figure 3.16 and Figure S3.10. In fact, the cross-equatorial transport around April and May 2022 (Figures 3.1c,d) is nearly absent in MIROC-CHASER, while evident in the other models as a small peak in the NH perturbation time series (see also Figure 3.16). The global stratospheric mixing timescales in WACCM6/CARMA, estimated from the convergence of global and hemispheric water vapour time series agree reasonably well with the 14 month timescale based on MLS observations (Figure 3.1d). In GEOSCCM, GEOS/CARMA, the time series converges near the end of the two-year simulation, suggesting a timescale of about 24 months. The mixing timescales in CAM5/CARMA, MIROC-CHASER, and LMDZ6.2-LR appear to be much longer, as seen from the separation between the northern and hemispheric averaged perturbations even at the end of 2023.

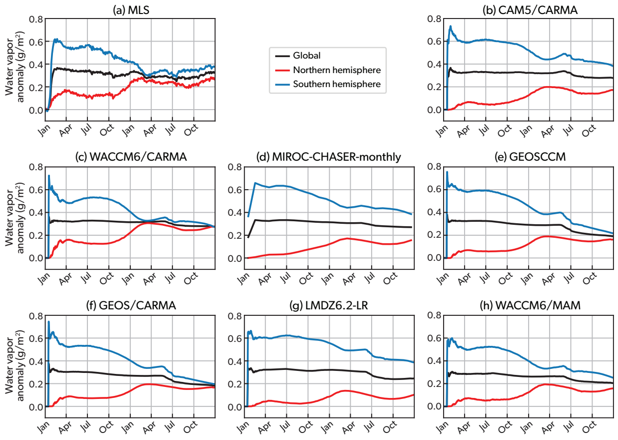

**Figure 3.21:** *Time series of Hunga water-vapour perturbations in global models from January 2022 to December 2023: global mean (black), Northern Hemisphere (red), and Southern Hemisphere (blue). Perturbations are calculated based on daily values, except for MIROC-CHASER, which uses monthly means. MLS-observed water vapour anomalies are calculated relative to January 2022 from deseasonalised values for 2022–2024.*

### 3.5.4 Summary of model performances

Overall, models reproduce the observed transport of water vapour and volcanic aerosols from the Hunga eruption quite well. Generally, the timing of the aerosol and water vapour transport outside of the tropics toward the southern hemisphere is represented remarkably well. Most models overestimate the early peak water vapour perturbation in the tropics with respect to MLS, but simulate well the water vapour perturbation after the first month from the eruption. Models also underestimate the peak SAOD with respect to OMPS (which, however, reports higher SAOD

values than other satellite instruments), indicating that the prescribed injection parameters need to be tuned. On the other hand, models simulate the decay rate of SAOD remarkably well, showing that the removal of aerosols through settling and circulation is generally well represented. In the second year after the eruption, the water vapour perturbation matches MLS observations very well, while the SAOD is still underestimated. All models underestimate the cross-equatorial transport compared to OMPS and confine most of the aerosols to the Southern Hemisphere.
All models simulate the vertical separation of water vapour and aerosols, with the water vapour ascending via the tropical upwelling branch of the Brewer-Dobson circulation and the aerosol remaining in the middle and lower stratosphere due to gravitational settling. The simulated period (2 years) was not long enough to derive the e-folding time of aerosols, which is tightly related to the aerosol effective radius. All models simulate an increase in aerosol particle size after the eruption. The aerosol size then decreases with time due to the faster settling of larger particles, and stabilises in all models around 0.2 - 0.3 µm, in agreement with observations.

## References

Asher, E., M. Todt, K. Rosenlof, T. Thornberry, R.-S. Gao, G. Taha, P. Walter, S. Alvarez, J. Flynn, S. M. Davis et al. (2023). 'Unexpectedly rapid aerosol formation in the Hunga Tonga plume'. *Proc. Natl. Acad. Sci.*, 120, e2219547120. DOI: `10.1073/pnas.2219547120`.

Boichu, M., R. Grandin, L. Blarel, B. Torres, Y. Derimian, P. Goloub, C. Brogniez, I. Chiapello, O. Dubovik, T. Mathurin et al. (2023). 'Growth and Global Persistence of Stratospheric Sulfate Aerosols From the 2022 Hunga Tonga–Hunga Ha'apai Volcanic Eruption'. *J. Geophys. Res.*, 128, e2023JD039010. DOI: `10.1029/2023JD039010`.

Bourassa, A. E., D. J. Zawada, L. A. Rieger, T. W. Warnock, M. Toohey and D. A. Degenstein (2023). 'Tomographic retrievals of Hunga Tonga-Hunga Ha'apai volcanic aerosol'. *Geophys. Res. Lett.*, 50, e2022GL101978. DOI: `10.1029/2022GL101978`.

Clyne, M., O. B. Toon, T. Sukhodolov, G. W. Mann, S. Dhomse, S. Tilmes, Y. Zhu, P. R. Colarco, K. Tsigaridis, T. Nagashima et al. (2024). 'Tonga-MIP: The Hunga Tonga-Hunga Ha'apai Volcano Model Intercomparison Project'. In M. Clyne (Ed.), *Modeling the role of volcanoes in the climate system* (Publication No. 31487034), `https://www.proquest.com/dissertations-theses/modeling-role-volcanoes-climate-system/docview/3100397790/se-2`. PhD thesis. University of Colorado at Boulder.

Duchamp, C., F. Wrana, B. Legras, P. Sellitto, R. Belhadji and C. von Savigny (2023). 'Observation of the aerosol plume from the 2022 Hunga Tonga–Hunga Ha'apai eruption with SAGE III/ISS'. *Geophys. Res. Lett.*, 50, e2023GL105076. DOI: `10.1029/2023GL105076`.

Global Volcanism Program (2024). *Volcanoes of the World (v. 5.2.8; 6 May 2025)*. Distributed by Smithsonian Institution, compiled by Venzke, E. DOI: `10.5479/si.GVP.VOTW5-2024.5.2`.

Khaykin, S., G. Taha, T. Leblanc, T. Sakai, I. Morino, B. Liley and S. Godin-Beekmann (2024). 'Stratospheric aerosols [in "State of the Climate in 2022"]'. *Bull. Am. Meteorol. Soc.*, 105, S96–S98. DOI: `10.1175/BAMS-D-24-0116.1`.

Khaykin, S., B. Legras, S. Bucci, P. Sellitto, L. Isaksen, F. Tencé, S. Bekki, A. Bourassa, L. Rieger, D. Zawada et al. (2020). 'The 2019/20 Australian wildfires generated a persistent smoke-charged vortex rising up to 35 km altitude'. *Commun. Earth Environ.*, 1, 22. DOI: `10.1038/s43247-020-00022-5`.

Khaykin, S., A. Podglajen, F. Ploeger, J.-U. Grooß, F. Tence, S. Bekki, K. Khlopenkov, K. Bedka, L. Rieger, A. Baron et al. (2022). 'Global perturbation of stratospheric water and aerosol burden by Hunga eruption'. *Commun. Earth Environ.*, 3, 316. DOI: `10.1038/s43247-022-00652-x`.

Knepp, T. N., M. Kovilakam, L. Thomason and S. J. Miller (2024). 'Characterization of stratospheric particle size distribution uncertainties using SAGE II and SAGE III/ISS extinction spectra'. *Atmos. Meas. Tech.*, 17, pp. 2025–2054. DOI: `10.5194/amt-17-2025-2024`.

Kovilakam, M., L. W. Thomason, N. Ernest, L. Rieger, A. Bourassa and L. Millán (2020). 'The Global Space-based Stratospheric Aerosol Climatology (version 2.0): 1979–2018'. *Earth Syst. Sci. Data*, 12, pp. 2607–2634. DOI: `10.5194/essd-12-2607-2020`.

Kovilakam, M., L. W. Thomason, M. Verkerk, T. Aubry and T. N. Knepp (2025). 'OMPS-LP aerosol extinction coefficients and their applicability in GloSSAC'. *Atmos. Chem. Phys.*, 25, pp. 535–553. DOI: `10.5194/acp-25-535-2025`.

Lawrence, Z. D., G. L. Manney and K. Wargan (2018). 'Reanalysis intercomparisons of stratospheric polar processing diagnostics'. *Atmos. Chem. Phys.*, 18, pp. 13547–13579. DOI: `10.5194/acp-18-13547-2018`.

Lee, S., G. L. Manney and A. H. Butler (2024). 'The 2023 Major Sudden Stratospheric Warming [in "State of the Climate in 2023"]'. *Bull. Am. Meteorol. Soc.*, 105, S288–S289. DOI: `10.1175/BAMS-D-24-0101.1`.

Li, C., Y. Peng, E. Asher, A. A. Baron, M. Todt, T. D. Thornberry, S. Evan, J. Brioude, P. Smale, R. Querel et al. (2024). 'Microphysical Simulation of the 2022 Hunga Volcano Eruption Using a Sectional Aerosol Model'. *Geophys. Res. Lett.*, 51, e2024GL108522. DOI: `10.1029/2024GL108522`.

Manney, G. L., M. L. Santee, A. Lambert, L. F. Millán, K. Minschwaner, F. Werner, Z. D. Lawrence, W. G. Read, N. J. Livesey and T. Wang (2023). 'Siege in the Southern Stratosphere: Hunga Tonga-Hunga Ha'apai Water Vapor Excluded From the 2022 Antarctic Polar Vortex'. *Geophys. Res. Lett.*, 50. DOI: `10.1029/2023gl103855`.

Millán, L., W. G. Read, M. L. Santee, A. Lambert, G. L. Manney, J. L. Neu, M. C. Pitts, F. Werner, N. J. Livesey and M. J. Schwartz (2024). 'The Evolution of the Hunga Hydration in a Moistening Stratosphere'. *Geophys. Res. Lett.*, 51, e2024GL110841. DOI: `10.1029/2024gl110841`.

NASA/LARC/SD/ASDC (2023). *Global Space-based Stratospheric Aerosol Climatology Version 2.21.* Data set. NASA Langley Atmospheric Science Data Center DAAC. DOI: `10.5067/GLOSSAC-L3-V2.21`.

Newman, P. A., L. R. Lait, N. A. Kramarova, L. Coy, S. M. Frith, L. D. Oman and S. S. Dhomse (2024). 'Record High March 2024 Arctic Total Column Ozone'. *Geophys. Res. Lett.*, 51, e2024GL110924. DOI: `10.1029/2024gl110924`.

Peter, T. (1997). 'Microphysics and heterogeneous chemistry of polar startospheric clouds'. *Annu. Rev. Phys. Chem.*, 48, pp. 785–822. DOI: `10.1146/annurev.physchem.48.1.785`.

Pitts, M. C., L. R. Poole and R. Gonzalez (2018). 'Polar stratospheric cloud climatology based on CALIPSO spaceborne lidar measurements from 2006 to 2017'. *Atmos. Chem. Phys.*, 18, pp. 10881–10913. DOI: `10.5194/acp-18-10881-2018`.

Polvani, L. M., D. W. Waugh and R. A. Plumb (1995). 'On the Subtropical Edge of the Stratospheric Surf Zone'. *J. Atmos. Sci.*, 52, pp. 1288–1309. DOI: `10.1175/1520-0469(1995)052<1288:otseot>2.0.co;2`.

Quaglia, I., D. Visioni, E. M. Bednarz, Y. Zhu, G. Stenchikov, V. Aquila, C.-C. Liu, G. W. Mann, Y. Peng, T. Sekiya et al. (2025). 'Multi-model analysis of the radiative impacts of the 2022 Hunga eruption indicates a significant cooling contribution from the volcanic plume'. *EGUsphere [preprint]*, 2025, pp. 1–35. DOI: `10.5194/egusphere-2025-3769`.

Rieger, L. A., A. E. Bourassa and D. A. Degenstein (2014). 'Stratospheric aerosol particle size information in Odin-OSIRIS limb scatter spectra'. *Atmos. Meas. Tech.*, 7, pp. 507–522. DOI: `10.5194/amt-7-507-2014`.

Rieger, L. A., D. J. Zawada, A. E. Bourassa and D. A. Degenstein (2019). 'A Multiwavelength Retrieval Approach for Improved OSIRIS Aerosol Extinction Retrievals'. *J. Geophys. Res.*, 124, pp. 7286–7307. DOI: `10.1029/2018jd029897`.

Rozanov, A., C. Pohl, C. Arosio, A. Bourassa, K. Bramstedt, E. Malinina, L. Rieger and J. P. Burrows (2024). 'Retrieval of stratospheric aerosol extinction coefficients from sun-normalized Ozone Mapper and Profiler Suite Limb Profiler (OMPS-LP) measurements'. *Atmos. Meas. Tech.*, 17, pp. 6677–6695. DOI: `10.5194/amt-17-6677-2024`.

Russell, P. B., J. M. Livingston, R. F. Pueschel, J. J. Bauman, J. B. Pollack, S. L. Brooks, P. Hamill, L. W. Thomason, L. L. Stowe, T. Deshler et al. (1996). 'Global to microscale evolution of the Pinatubo volcanic aerosol derived from diverse measurements and analyses'. *J. Geophys. Res.*, 101, pp. 18745–18763. DOI: `10.1029/96jd01162`.

Santee, M. L., G. L. Manney, A. Lambert, L. F. Millán, N. J. Livesey, M. C. Pitts, L. Froidevaux, W. G. Read and R. A. Fuller (2024). 'The Influence of Stratospheric Hydration From the Hunga Eruption on Chemical Processing in the 2023 Antarctic Vortex'. *J. Geophys. Res.*, 129, e2023JD040687. DOI: `10.1029/2023jd040687`.

Schoeberl, M. R., Y. Wang, R. Ueyama, G. Taha, E. Jensen and W. Yu (2022). 'Analysis and Impact of the Hunga Tonga-Hunga Ha'apai Stratospheric Water Vapor Plume'. *Geophys. Res. Lett.*, 49, e2022GL100248. DOI: `10.1029/2022gl100248`.

Sellitto, P., A. Podglajen, R. Belhadji, M. Boichu, E. Carboni, J. Cuesta, C. Duchamp, C. Kloss, R. Siddans, N. Bègue et al. (2022). 'The unexpected radiative impact of the Hunga Tonga eruption of 15th January 2022'. *Commun. Earth Environ.*, 3, 288. DOI: `10.1038/s43247-022-00618-z`.

Sonnemann, G. R. and M. Grygalashvyly (2005). 'Solar influence on mesospheric water vapor with impact on NLCs'. *J. Atmos. Solar-Terr. Phys.*, 67, pp. 177–190. DOI: `10.1016/j.jastp.2004.07.026`.

Taha, G., R. Loughman, T. Zhu, L. Thomason, J. Kar, L. Rieger and A. Bourassa (2021). 'OMPS LP Version 2.0 multi-wavelength aerosol extinction coefficient retrieval algorithm'. *Atmos. Meas. Tech.*, 14, pp. 1015–1036. DOI: `10.5194/amt-14-1015-2021`.

Thomason, L. W., N. Ernest, L. Millán, L. Rieger, A. Bourassa, J.-P. Vernier, G. Manney, B. Luo, F. Arfeuille and T. Peter (2018). 'A global space-based stratospheric aerosol climatology: 1979–2016'. *Earth Syst. Sci. Data*, 10, pp. 469–492. DOI: `10.5194/essd-10-469-2018`.

Tritscher, I., M. C. Pitts, L. R. Poole, S. P. Alexander, F. Cairo, M. P. Chipperfield, J.-U. Grooß, M. Höpfner, A. Lambert, B. Luo et al. (2021). 'Polar Stratospheric Clouds: Satellite Observations, Processes, and Role in Ozone Depletion'. *Rev. Geophys.*, 59, e2020RG000702. DOI: `10.1029/2020rg000702`.

Wohltmann, I., M. L. Santee, G. L. Manney and L. F. Millán (2024). 'The Chemical Effect of Increased Water Vapor From the Hunga Tonga-Hunga Ha'apai Eruption on the Antarctic Ozone Hole'. *Geophys. Res. Lett.*, 51, e2023GL106980. DOI: `10.1029/2023gl106980`.

Wrana, F., C. von Savigny, J. Zalach and L. W. Thomason (2021). 'Retrieval of stratospheric aerosol size distribution parameters using satellite solar occultation measurements at three wavelengths'. *Atmos. Meas. Tech.*, 14, pp. 2345–2357. DOI: `10.5194/amt-14-2345-2021`.

Xu, J., D. Li, Z. Bai, M. Tao and J. Bian (2022). 'Large Amounts of Water Vapor Were Injected into the Stratosphere by the Hunga Tonga–Hunga Ha'apai Volcano Eruption'. *Atmosphere*, 13, 912. DOI: `10.3390/atmos13060912`.

Zhou, X., S. S. Dhomse, W. Feng, G. Mann, S. Heddell, H. Pumphrey, B. J. Kerridge, B. Latter, R. Siddans, L. Ventress et al. (2024). 'Antarctic Vortex Dehydration in 2023 as a Substantial Removal Pathway for Hunga Tonga-Hunga Ha'apai Water Vapor'. *Geophys. Res. Lett.*, 51, e2023GL107630. DOI: `10.1029/2023gl107630`.

Zhu, Y., H. Akiyoshi, V. Aquila, E. Asher, E. M. Bednarz, S. Bekki, C. Brühl, A. H. Butler, P. Case, S. Chabrillat et al. (2025). 'Hunga Tonga–Hunga Ha'apai Volcano Impact Model Observation Comparison (HTHH-MOC) project: experiment protocol and model descriptions'. *Geosci. Model Dev.*, 18, pp. 5487–5512. DOI: `10.5194/gmd-18-5487-2025`.

Zhuo, Z., X. Wang, Y. Zhu, W. Yu, E. M. Bednarz, E. Fleming, P. R. Colarco, S. Watanabe, D. Plummer, G. Stenchikov et al. (2025). 'Comparing multi-model ensemble simulations with observations and decadal projections of upper atmospheric variations following the Hunga eruption'. *Atmos. Chem. Phys.*, 25, pp. 13161–13176. DOI: `10.5194/acp-25-13161-2025`.